AGU ADVANCING EARTH AND SPACE SCIENCES

JGR Space Physics

RESEARCH ARTICLE

10.1029/2023JA031712

Key Points:

- Geomagnetic storm phases, rather than geomagnetic indices alone, portray storm time electromagnetic ion cyclotron (EMIC) waves more effectively
- EMIC waves occur 2.9 times more frequently during storms than during non-storm times
- The storm time occurrence rate is highest during the pre-onset phase, followed by the main and recovery phases

Supporting Information:

Supporting Information may be found in the online version of this article.

Correspondence to:

B. Remya,
remyaphysics@gmail.com

Citation:

Remya, B., Halford, A. J., Sibeck, D. G., Murphy, K. R., & Fok, M.-C. (2023). Understanding quiet and storm time EMIC waves—Van Allen Probes results. *Journal of Geophysical Research: Space Physics*, *128*, e2023JA031712. https://doi.org/10.1029/2023JA031712

Received 1 JUN 2023
Accepted 17 JUL 2023

Author Contributions:

Conceptualization: B. Remya, A. J. Halford, D. G. Sibeck
Data curation: B. Remya
Formal analysis: B. Remya
Investigation: B. Remya
Methodology: B. Remya, K. R. Murphy
Validation: A. J. Halford
Writing – original draft: B. Remya
Writing – review & editing: B. Remya, A. J. Halford, D. G. Sibeck, K. R. Murphy, M.-C. Fok

Understanding Quiet and Storm Time EMIC Waves—Van Allen Probes Results

B. Remya[1], A. J. Halford[2], D. G. Sibeck[2], K. R. Murphy[3], and M.-C. Fok[2]

[1]Indian Institute of Geomagnetism, Navi Mumbai, India, [2]NASA Goddard Space Flight Center, Greenbelt, MD, USA, [3]Self-employed, Edmonton, AB, Canada

Abstract Geomagnetic indices have been used as a proxy for studying electromagnetic ion cyclotron (EMIC) wave occurrences under different geomagnetic conditions. However, the drivers of EMIC waves are different during non-storm, storm time and during individual storm phases. Using ~7 years of data from the twin Van Allen Probes, we demonstrate that the occurrence probability of EMIC waves are not well captured by a specific geomagnetic activity index alone, but is rather well manifested by considering individual storm phases. We show EMIC wave occurrence statistics during different storm phases (pre-onset, main and recovery) for geomagnetic activity indices Sym-H, AE, and *Kp* and solar wind dynamic pressure P_{dyn}, illustrating that the occurrence rates vary significantly during different storm phases even for a given geomagnetic index. We also utilize this large database to show EMIC wave occurrence distribution, and how various wave and plasma parameters behave under different geomagnetic conditions. EMIC waves occur 2.9 times more often during geomagnetic storms than during non-storm times. The majority (72%) of storm time EMIC waves occur during the recovery phase due to long recovering time, while the highest occurrence rates are in the pre-onset phase, followed by main and recovery phases. EMIC waves in the main phase have occurrence peaks in the dusk to pre-midnight sectors while recovery phase events spread to more Magnetic Local Time (MLT) sectors with peaks in the morning sector. Wave amplitudes are found to be evenly distributed across different MLT sectors during all geomagnetic conditions.

1. Introduction

Electromagnetic ion cyclotron (EMIC) waves are discrete electromagnetic emissions identified as transverse, left-hand polarized waves in the frequency range of 0.1–5 Hz (Pc1-Pc2 band) (Jacobs et al., 1964). They are believed to be generated in the Earth's magnetosphere by temperature anisotropies $T_\perp/T_\parallel > 1$, which can be produced during periods of enhancements of ~10–100 keV energy ring current protons overlapping with a cold dense plasma population (e.g., Cornwall, 1965; Kennel & Petschek, 1966) or due to solar wind compression of the dayside magnetosphere by interplanetary shocks or solar wind pressure enhancements (e.g., Olson & Lee, 1983). While anisotropic hot ions act as free energy source for EMIC wave generation, the cold plasma population is thought to enhance wave growth rates (Rauch & Roux, 1982; Young et al., 1981). The preferred region for EMIC wave generation is near the geomagnetic equator (minimum magnetic field regions) where the wave vector is parallel and minimum along the magnetic field (Kozyra et al., 1984; Loto'aniu et al., 2005). EMIC waves can also be generated off-equator when the magnetic field reconfigures during dayside compressions forming Shabansky orbits (Allen et al., 2015; McCollough et al., 2012; Shabansky, 1971).

EMIC waves have been observed over varied L-shells ($L = 3$ to $L = 14$) and over almost all Magnetic Local Time (MLT) regions. A number of studies using different in-situ missions have characterized the magnetospheric distribution of EMIC wave, occurrence as a function of L-shell and MLT, wave properties, and their dependence on geomagnetic conditions. For example, Anderson and Hamilton (1993) and Keika et al. (2013) (Active Magnetospheric Particle Tracer Explorers (AMPTE)/CCE), Engebretson et al. (2002) (Polar), Allen et al. (2015) (Cluster), J.-S. Park et al. (2016); Fraser et al. (2010) (GOES), Halford et al. (2010, 2016) and Meredith et al. (2014) (Combined Radiation Release and Effects Satellite (CRRES)), Min et al. (2012) and Usanova et al. (2012) (THEMIS), Saikin et al. (2015) and D. Wang et al. (2015) (Van Allen Probes), X. Y. Wang et al. (2017) (MMS), to name a few. Most of the previous studies using different in-situ observations consistently show that peak occurrence rate for EMIC waves is in the pre-noon to dusk sector (0900–1800 MLT) in the outer magnetosphere. Smaller but significant occurrence peaks are also observed at dawn sector between 0300 and 0900 MLT in the outer magnetosphere ($L > 10$) (Allen et al., 2015; Min et al., 2012; Usanova et al., 2012). This

10.1029/2023JA031712

dawn sector occurrence peak at higher L-shells is strongly correlated with the dayside magnetospheric compressions (high pressure). Interestingly, the dawn sector occurrence peak at lower L-shells was not identified by Saikin et al. (2015) but was observed by D. Wang et al. (2015), though both results are from Van Allen Probes mission. Majority of the studies show consistent results with each other. Some of the minor differences among these results can be attributed largely to the orbit and sensitivity of the magnetometers on the satellites as well as to the identification process of the waves used in different studies.

EMIC waves are known to be an important player in ring current and radiation belt dynamics as they can pitch angle scatter ring current ions (Cornwall et al., 1970; Jordanova et al., 2001; Kennel & Petschek, 1966) and radiation belt relativistic electrons (Fraser et al., 2010; Miyoshi et al., 2008; Su et al., 2013; Shumko et al., 2022; Summers & Thorne, 2003; Summers et al., 2007b; Thorne, 2010; Ukhorskiy et al., 2010; J. Zhang et al., 2016) to the ionosphere or atmosphere thereby contributing to the magnetospheric loss processes. EMIC waves are also known to heat low energy (eVs) ions to keVs of energies via wave-particle interactions (J.-C. Zhang et al., 2010). Thus the relationship of EMIC waves with geomagnetic storms have been of great research interest in the past few decades. Several studies, both satellite and ground based, have investigated the relation between EMIC wave occurrence and geomagnetic activity (Bortnik et al., 2008; Bräysy et al., 1998; Erlandson & Ukhorskiy, 2001; Engebretson et al., 2008; Fraser et al., 2010; Halford et al., 2010; Keika et al., 2013; Meredith et al., 2014; Saikin et al., 2016; Usanova et al., 2012; D. Wang et al., 2016; Wentworth, 1964).

Erlandson and Ukhorskiy (2001) using 10 years of observations from the Dynamic Explorer 1 (DE 1) satellite found that EMIC waves are 5 times more likely to occur during geomagnetic storms than during quiet times in the equatorial magnetosphere. Using the CRRES data Halford et al. (2010) show that EMIC waves are 1.6 times more likely to occur during storms than during non-storm times with maximum occurrence rates during the main phase. Another study Meredith et al. (2014), also using CRRES observations, show peak occurrence rates for noon time EMIC waves during disturbed periods (AE > 300). Usanova et al. (2012) found higher EMIC wave occurrence in the outer magnetosphere associated with high *AE*. Due to the high altitude of the satellite, their study focuses mostly on the outer magnetosphere and hence reports low (<10%) storm time occurrence in the inner magnetosphere. Also, because their study interval covered low solar activity (solar minimum) period, they had fewer storm time intervals. More recently, results from the first precession of the Van Allen Probes satellites reported EMIC wave occurrence rate during storm time is 2.8 times than that during the non-storm time (D. Wang et al., 2016).

Keika et al. (2013) used AMPTE/CCE satellite observations during its whole mission period of ∼4.5 years and found that majority of storm time waves in the He^+ band occurred during the main phase of storms with its peak occurrence in the afternoon in the outer magnetosphere $L > 7$. Results from Fraser et al. (2010) from GOES observations at geosynchronous orbits showed that EMIC waves were present during the main phase in 13 of the 22 storms they studied. Major storm time EMIC events are found to occur in the noon to dusk region and is consistent in all of the above studies. Modeling studies (Jordanova et al., 2001; Khazanov et al., 2006) agree well with observational results suggesting that EMIC waves peak during the onset and main phase of a geomagnetic storm.

Contrary to satellite observations, the Pc-1 and Pc-2 geomagnetic pulsations, which are the ground based signatures of EMIC waves are observed with higher occurrence frequently during the recovery phase (Engebretson et al., 2008; Fraser et al., 2010). This is plausibly due to the broadband precipitation on the ground during the storm main phase which may mask the EMIC wave frequencies (Bortnik et al., 2008; Engebretson et al., 2008). EMIC waves may also be more strongly attenuated in the ionosphere during the main phase of the storm.

Nevertheless, not all storms are observed to have EMIC waves. This is likely due to the lack of consistent and complete coverage of the magnetosphere during a single geomagnetic storm. Therefore, storm-time dependence and more specifically storm-phase dependence of EMIC waves still remains unclear. Questions like whether EMIC waves are more often observed during storm times or non-storm periods and how the EMIC wave occurrence pattern, wave amplitude, and plasma parameters vary during different storm phases need to be understood to incorporate them in global MHD models. Hence, a comprehensive statistical analysis is warranted to understand when and where these waves occur. It will only be possible for a single satellite mission to answer some of the questions on a global scale. Nevertheless, studies using different satellite missions covering different solar activity intervals can add up to provide the spatial coverage necessary for converging the statistics and help provide a better understanding of the active region of EMIC waves during an individual storm.

The present paper expands upon past reports to investigate EMIC waves in the inner magnetosphere. We use ∼7 years of Van Allen Probes mission data and attempt to address the following questions: (a) Are geomagnetic indices a good/sufficient proxy for EMIC waves? (b) Whether EMIC wave occurrence probability is higher during quiet or storm time? (c) What are the storm time dynamics of EMIC waves - how does the wave occurrence pattern and wave parameters change during individual storm phases, which phase has higher occurrence rate and why? In this paper we analyze the occurrence rates of EMIC waves with respect to geomagnetic indices and storm phases to show that geomagnetic indices do not provide a good characterization of the occurrence of EMIC waves. We will then consider typical wave and plasma parameters during the Van Allen Probe mission under different geomagnetic conditions and storm phases. In addition, we compare our results with previous statistical studies and evaluate new and existing knowledge on EMIC wave occurrence in the Earth's inner magnetosphere.

The paper is organized in the following manner: Section 2 discusses the data and methodology where we give a description of the Van Allen Probe data and the analysis technique used for detecting EMIC waves. Section 3 focuses on the detailed statistical results on occurrence and wave power distribution of EMIC waves during various geomagnetic activity and storm phases. This is followed by a Discussion section where we compare our results with all past statistical studies (Section 4). The paper culminates with a Summary and Conclusion (Section 5) of the results.

2. Data Analysis and Methodology

2.1. Van Allen Probes

Van Allen Probes (previously named Radiation Belt Storm Probes, RBSP) mission (Mauk et al., 2013), launched on 30 August 2012 with an apogee of nearly $5.8R_E$ and a perigee of $\sim 1.1R_E$, provides an excellent opportunity to study the EMIC wave distribution in the inner magnetosphere. The twin spacecraft, denoted as A and B, are identically instrumented and follow nearly identical highly elliptical orbits with low inclination (∼10°). Their orbital apogees differ by ∼130 km which causes one spacecraft to lap the other every ∼75 days. The low inclination along with the tilt of the Earth's magnetic axis enables sampling over $-20° \leq$ MLAT $\leq 20°$. In this study, we use Van Allen Probes' high resolution (64 Hz) magnetometer data from Electric and Magnetic Field Instrument Suite and Integrated Science (EMFISIS) suite (Kletzing et al., 2013) for EMIC wave detection. The Energetic Particle, Composition, and Thermal Plasma (ECT) suite (Spence et al., 2013) provides measurements of energetic ions in the ring current. The location of EMIC wave events in terms of L-shell, MLT and MLAT are obtained from estimated measurements onboard ECT/Magnetic Electron Ion Spectrometer instrument (Blake et al., 2013). Additionally, electron density data estimated from the spacecraft potential is obtained from Electric Field and Waves (EFW) instrument (Wygant et al., 2013) on Van Allen Probes. For intervals without EFW density data, we use density values determined from the EMFISIS upper hybrid line. If there are no density measurements available for a specific duration, we omit those intervals from our study. We examine EMIC wave events observed by both Van Allen Probes A and B (denoted as RBSP-A and RBSP-B) during a period from September 2012 to July 2019 (∼7 years). The mission was operational during solar cycle 24 with its peak in April 2014.

2.2. Geomagnetic Conditions

To identify geomagnetic storms, we use the *Sym-H* index from the OMNI solar wind and geomagnetic indices database at 1-min cadence. We identify 144 geomagnetic storms during the period from September 2012 to July 2019 using the initial criteria described by Murphy et al. (2018). The algorithm determines a storm start and end time, t_{-1} and t_1, respectively, and an epoch time t_0. Murphy et al. (2018) identifies the start time of the storm as the start of an enhanced solar wind driving and uses *Dst* index (1 hr cadence) to find the epoch time t_0. The detailed criteria for identifying the start and end time of the storms are described in the Supporting Information for Murphy et al. (2018). As our study focuses on individual storm phases and need a start time for the pre-onset, main and recovery phases, we further modify the initial list of storms derived by Murphy et al. (2018) to identify the start and end times of the individual storm phases. For this, we use *Sym-H* index to determine a more specific epoch time t_{min} as *Sym-H* index is a higher temporal version of the 1 hr *Dst* index. Hence it will serve as a better proxy for the strength of the ring current and would capture the dayside compressions better, both of which are known to be major drivers of EMIC waves. Also, as EMIC wave intervals typically last for few minutes to sometimes a few hours, the *Sym-H* index will be an ideal candidate for EMIC wave studies.

In our study, the storm main phases are characterized by localized minima satisfying $Sym\text{-}H < -50$ nT. We define the epoch time, t_{min} as the time of minimum *Sym-H* between the interval t_{-1} and t_1. This t_{min} is the end time of the

10.1029/2023JA031712

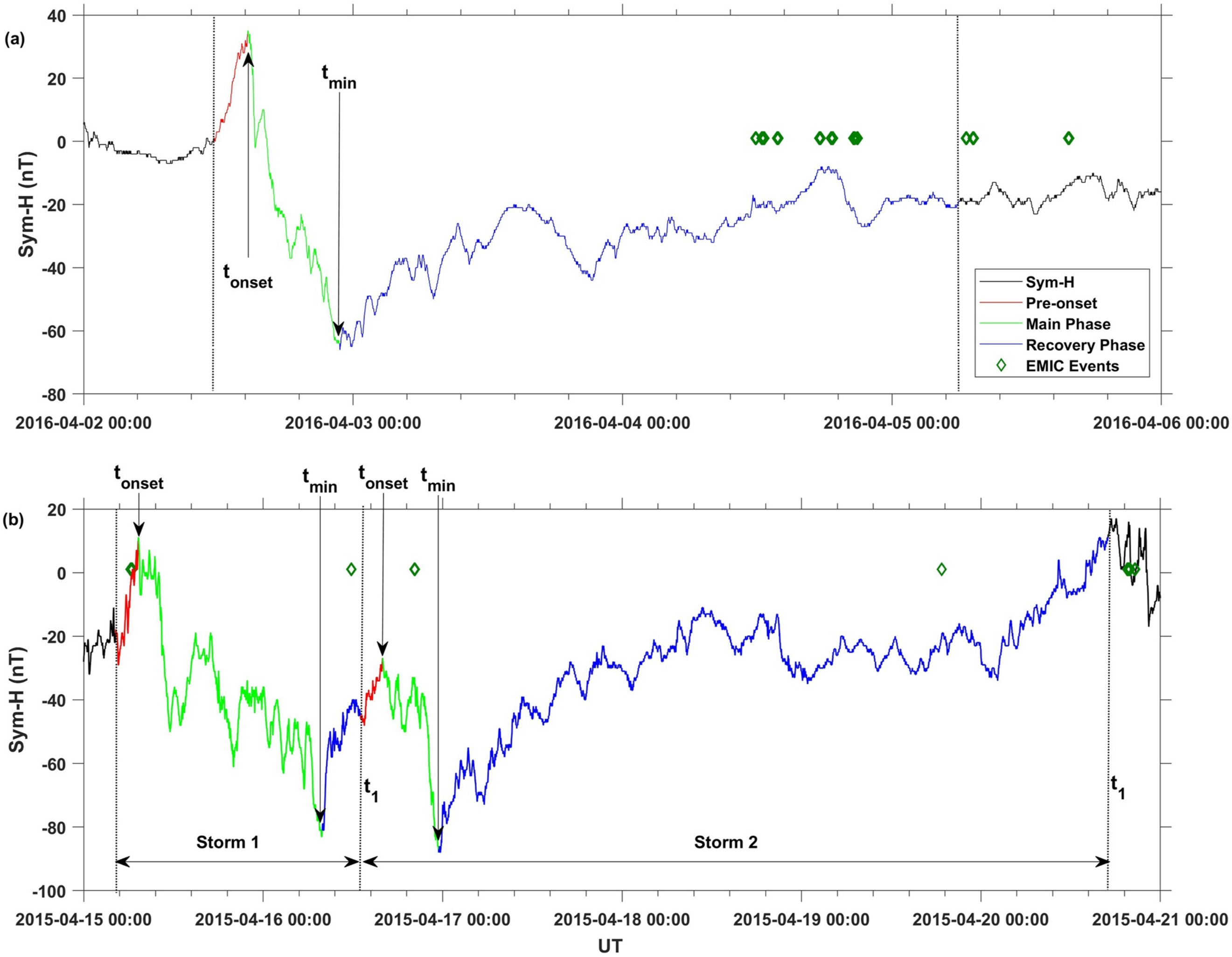

Figure 1. An example of how (a) typical storm and (b) double dip storm is identified in the present study. The black dotted lines indicate the start and end time of the corresponding storm and the arrows indicate times t_{onset}, $t_{\min}$, and t_1 for individual storm.

main phase. To determine the start of main phase, we find a peak in *Sym-H* between t_{-1} and $t_{\min}$. For storms that are driven by Coronal Mass Ejections (CMEs), the storm onset is clearly marked as a sudden storm commencement or a sudden impulse (SI) in the *Sym-H* index. If such a demarcation is not clearly visible, we use localized peaks in *Sym-H* index with *Sym-H* > 0 and use the last such peak as the storm onset, that is, start of the main phase. If *Sym-H* < 0 in the interval t_{-1} to $t_{\min}$, then we use the earlier peak as the storm onset time (t_{onset}).

The pre-onset period is defined as ~3 hr prior to the storm onset. Period from onset to minimum *Sym-H* is defined as main phase, while recovery phase begins after the minimum *Sym-H* and ends at time t_1 defined in Murphy et al. (2018) when enhanced solar wind driving has stopped. The end of the enhanced solar wind driving is defined when solar wind velocity and solar wind dynamic pressure have dropped below enhanced conditions for longer than a day. The storm time solar wind driving is expected to have stopped by then. The end of recovery phase is then defined as the time of recovery of *Dst*—t_1 (Refer to Murphy et al. (2018) for detailed description of the storm phase identification). If there is a double dip (e.g., 15–21 April 2015) or multi-dip (e.g., 07–16 October 2012) storm, we consider them as separate events unlike Murphy et al. (2018). In such cases, the end of the recovery phase and the pre-onset of the next storm will have an overlap of 3 hr duration. Figure 1 shows examples of (a) how a typical storm in our study looks like and (b) how double dip storms are separated. The start and end of the storm (t_1) are marked by black dotted lines. Arrows in the panels point to the onset time t_{onset} and time of minimum *Sym-H* $t_{\min}$. The green diamonds indicate where EMIC wave events are identified during the storm. The epoch times and corresponding *Sym-H* minima for the 144 geomagnetic storms identified between September 2012 and July 2019 are listed as Data Set S1.

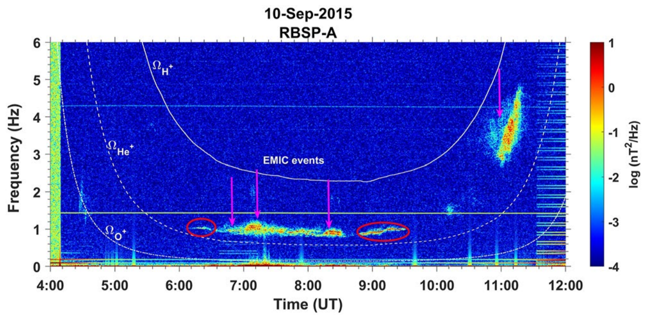

Figure 2. An example of a Van Allen Probe orbit showing dynamic spectra used to identify EMIC waves. The three white lines are the Hydrogen, Helium, and Oxygen cyclotron frequencies observed by Van Allen Probes.

2.3. EMIC Waves

We identify EMIC wave events with $L > 2$ in the study interval using an automated wave detection algorithm primarily based on (Bortnik et al., 2007). The 64 Hz vector magnetic field measurements are processed in 1 hr intervals. The wavefield, after removing the background field, are processed through Fast Fourier Transform to obtain the dynamic spectrogram for each 1 hr interval. A 100s (6,400 points) window length with an overlap of 80s (5,120 points) is used which provides a 0.01 Hz frequency resolution and 20s time resolution. For our study, we consider a fluctuation to be an EMIC wave event only if its power content is 1 order of magnitude greater than the background noise level in the corresponding 1 hour data interval. A lower and upper cut off frequency is set depending on the gyrofrequencies of proton and oxygen at geomagnetic equator, only to reduce the size of the spectrograms. The algorithm is hence set to identify waves if the wave activity was observed with frequencies between $0.1 < fq < 10$ Hz. We set a minimum time resolution of 3-min between any two adjacent wave events. Also, events with temporal length of less than 4-min are excluded so as to avoid picking up isolated peaks. A minimum and maximum spectral width of $0.1 < \delta f < 8$ Hz is also set to avoid picking up false positives and broadband activities.

Figure 2 shows an orbit of RBSP-A where EMIC waves are identified using the algorithm. The pink arrows shows the waves identified by the algorithm and the ones in the red circles were the missed ones. The two events missed by the algorithm had spectral widths $\delta f < 0.1$ Hz and hence were not listed as EMIC events due to the minimum spectral width criteria in our algorithm. Hence the start time of the observed/identified wave event was ~06:48UT which lasted as a series until 08:28UT spread over frequencies 0.8–1.25 Hz. Another wave event started at 10:53UT until ~11:18UT and spread across 2.6–4.8 Hz frequencies.

The algorithm documents the frequency, wave power, amplitude, start and end time and L/MLT/MLAT values of all efficient EMIC wave events into a wave list. Wave events are further manually verified by double-checking each spectrogram to avoid any false identification. Our algorithm identified a total of 3,206 EMIC waves throughout the Van Allen Probes era. However, further visual inspection of wave spectrum discerned several broadband events included in the list. Broadband wave activity has been excluded from the list of EMIC wave events. The remaining 2,442 EMIC wave events (totaling 30,020 min) is used for the current statistical study. Information on multi-band events are also recorded but are considered as a single event in the present study.

3. Statistical Results

The present paper illustrates EMIC wave occurrence distribution, wave and plasma parameters, and key geomagnetic parameters/indices during the quiet and storm time as well as for individual storm phases. We use a comprehensive data set of ~7 years during the Van Allen Probes era from September 2012 to July 2019 amounting to a study duration 3,601,439 min from both probes A and B. A total of 144 geomagnetic storms have been identified in this interval with a time duration of 973,785 min which accounted as ~27% of the total study duration. The average length of the storms in our study is 112.5 hr with mean lengths of main and recovery phases as 19 and 90.5 hr, respectively. EMIC waves were found to be present during 131 of 144 (91%) identified storms. A total of 2,442 EMIC events were identified throughout our study period which accounted for 30,020 min of wave activity. Out of these, 15,548 min (~52%) of EMIC wave activity occurred during storm time and remaining ~48% (14,472 min) during quiet times (Ref. Table 3). The occurrence rate of EMIC waves during geomagnetic storms can be hence obtained as the total duration of EMIC waves during storms divided by the total storm duration, which is found to be 1.6%. Similarly, occurrence rate of EMIC waves during geomagnetic quiet times is found to be 0.55%. The EMIC wave occurrence during storm times is therefore 2.9 times more often than during quiet times.

3.1. Are Geomagnetic Indices a Good Proxy for EMIC Waves?

Geomagnetic indices are strong indicators of the severity of geomagnetic activity. For instance, decreased negative values of *Dst*/*Sym-H* indicate geomagnetic storms as they respond to the strengths of the symmetric and asymmetric ring current and tail current in the Earth's magnetosphere (Rostoker, 1972; Sckopke, 1966; Sugiura, 1964). Likewise, Auroral indices like *AE* index are better indicators of steady magnetospheric convection and substorm

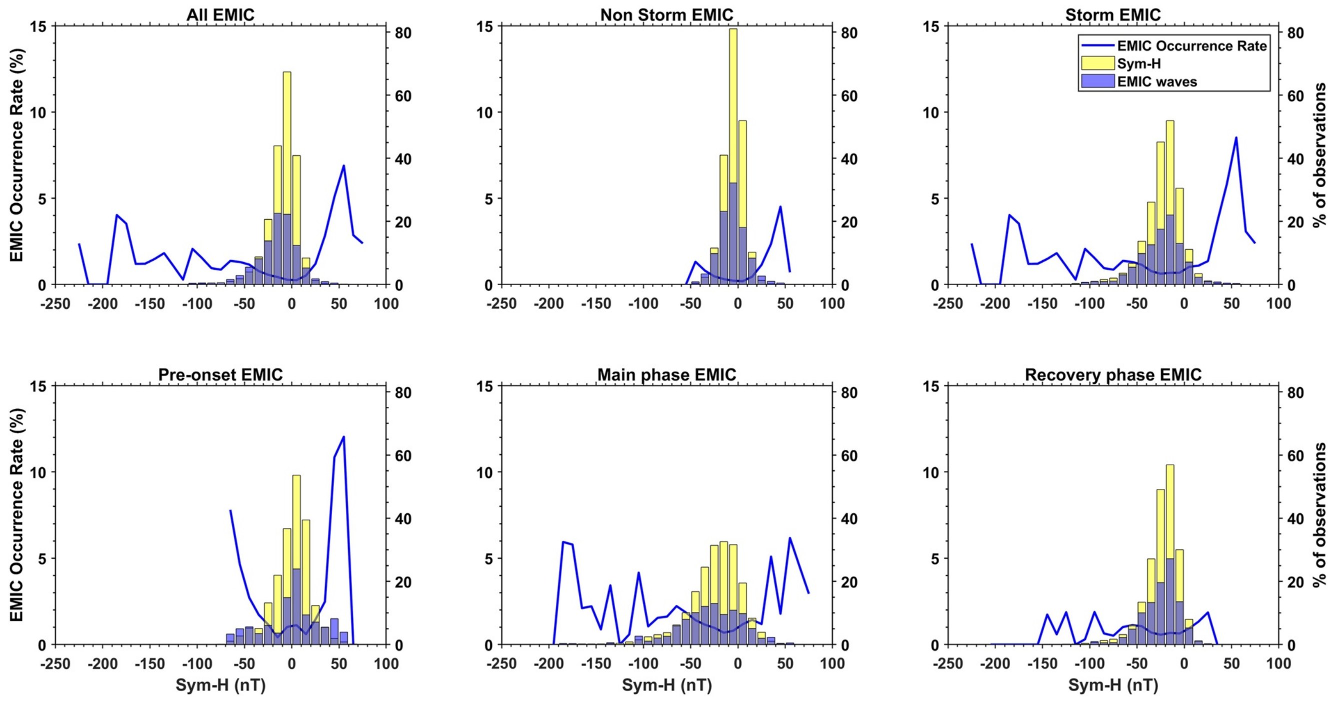

Figure 3. Occurrence rate of EMIC waves (blue lines) for a given *Sym-H* bin for all, non-storm and storm periods, and during the pre-onset, main, and recovery phases. The blue and yellow bars indicate percentage of EMIC waves and *Sym-H* observations in a given bin, respectively.

activity (Davis & Sugiura, 1966; Kamide & Akasofu, 1983; Rostoker, 1972). The planetary K-index, *Kp*, is a strong manifestation of magnetospheric convection (Thomsen, 2004). However, each of these indices can be greatly affected by other magnetospheric and ground induced current systems. For example, *Kp* index includes contribution from both ring current and auroral electrojets. Nevertheless, as varying geomagnetic activity levels affect the dynamics of the magnetosphere, geomagnetic indices have long been used to study wave distribution, wave occurrence rates and thereby wave-particle interactions in the Earth's magnetosphere (Chen et al., 2019; Kasahara et al., 1992; Keika et al., 2013; Li et al., 2009; Meredith et al., 2014; J. Park et al., 2013; Saikin et al., 2016; Usanova et al., 2012).

In particular, with reference to EMIC waves, geomagnetic storms and substorms drive anisotropic ion injections into the Earth's ring current which can in turn drive EMIC waves if the amount of free energy injected is sufficient (Blum et al., 2009, 2015; Erlandson & Ukhorskiy, 2001; Remya et al., 2018). Such injections can be manifested by the *AE* index (substorms) or the *Sym-H*/*Dst* indices (storms). Overall, several geomagnetic indices have been used to characterize the occurrence and distribution of EMIC waves in several past studies (Keika et al., 2013; Meredith et al., 2014; Saikin et al., 2015; Usanova et al., 2012). However, it is important to ask if geomagnetic indices alone are sufficient to describe either the occurrence of EMIC waves or the wave properties themselves (e.g., amplitude). The drivers and hence the physics of generation of EMIC waves differ during different geomagnetic conditions. This is because the local plasma conditions like particle parallel temperature, ion temperature anisotropy, ion composition, ion densities, etc., in the magnetosphere are different during the different storm phases even for a given value of geomagnetic index. This also highlights the fact that the wave and particle dynamics need to be studied simultaneously to fully understand the physics associated with the wave-particle dynamics during each geomagnetic condition. As same values of *AE*, *Sym-H* and *Kp* index can be found during quiet, pre-onset, main, and recovery phases (for e.g., see Figure 1 of Halford et al. (2016)), it is rather crucial that we take into account not just the geomagnetic indices but also the local plasma and field conditions during each geomagnetic condition.

Figures 3 and 4 depict the occurrence rates of EMIC waves for a given value of geomagnetic index, *Sym-H*, and *AE*, respectively. The different panels show occurrence rate (blue lines) calculated for all, non-storm and storm time EMIC and during individual storm phases. The occurrence rate is calculated as the duration of EMIC activity in each index bin divided by the total satellite dwell time in that bin (in minutes) during individual geomagnetic condition. A specific bin is considered to be statistically valid if Van Allen Probes had a dwell time of at least

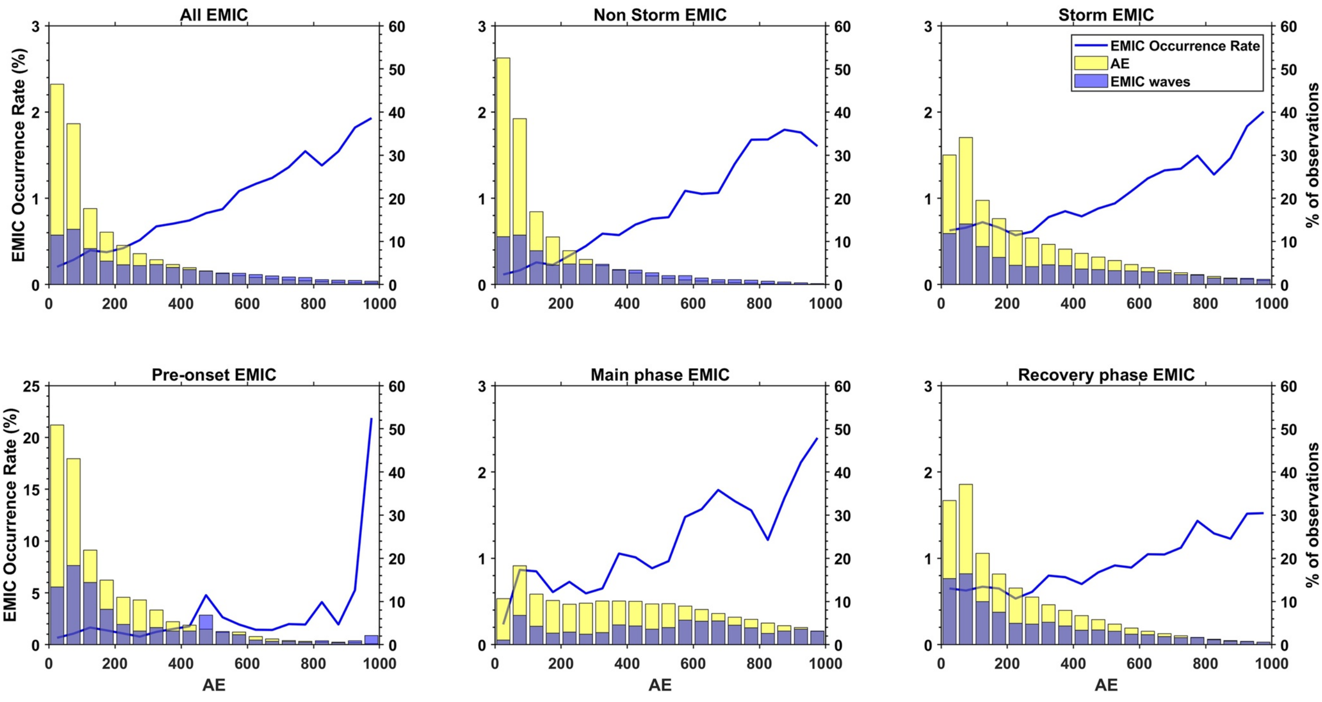

Figure 4. Occurrence rate of EMIC waves (blue lines) for a given *AE* bin for all, non-storm and storm periods, and during the pre-onset, main, and recovery phases. The blue and yellow bars indicate percentage of EMIC waves and *AE* observations in a given bin, respectively.

40 min in that bin (same criteria as Halford et al. (2016)). The normalized number of observations of each index, *Sym-H* and *AE*, for each bin during the given geomagnetic condition are displayed as yellow bars (in percentage) in the panels. This will help us to evaluate how often a given index value appears in each storm phase. The percentage of EMIC wave observations in each bin is shown as blue bars for each panel. As is apparent, the EMIC wave occurrence distribution and the occurrence distribution of the indices vary during different geomagnetic conditions.

In Figure 3, the peak occurrence rate during storm time is 8.5% in the 50–60 nT *Sym-H* bin while the peak occurrence bin during non-storm time is nearly half of that (4.5%) in the 40–50 nT bin. The highest occurrence rate of 12% is obtained during pre-onset phase, followed by main phase (6.2%) and the minimum found during the recovery phase (1.9%). This indicates that maximum occurrence of EMIC waves are to be expected during magnetospheric compressions which is in good agreement with results from past studies (Allen et al., 2013; Anderson & Hamilton, 1993; Engebretson et al., 2002; Halford et al., 2016; Lessard et al., 2019; Min et al., 2012; Olson & Lee, 1983; J.-S. Park et al., 2016; Saikin et al., 2015; Usanova et al., 2012) where maximum occurrence is found at higher L-shells near noon sector where waves are believed to be generated due to solar wind dynamic pressure enhancements. Main phase occurrence rates are enhanced at very low (<-100 nT) and very high (>30 nT) *Sym-H* values. The former enhancement is due to the sudden increase in the ring current ions and the latter corresponds to the compression of the magnetosphere which extends into the main phase of a storm. The recovery phase sees lower occurrence rates as compared to main phase or storm time in general even for the same *Sym-H* bins. This is because, during the main phase, ring current is enhanced and has more free energy for EMIC waves whereas during the recovery phase, the ring current is decaying and so the amount of free energy for EMIC waves is less. This indicates that at a given value of *Sym-H*, even with uniform measure of ring current in different storm phases, the occurrence of waves are not necessarily the same. This corroborates the idea that geomagnetic indices alone are not a good proxy for EMIC wave occurrence. Rather, coupling indices with storm phases provides a more complete picture of EMIC waves occurrence as it in part accounts for changes in the free energy available in the system.

EMIC wave occurrence has been associated with ion injections during substorms (Blum et al., 2015; Remya et al., 2018, 2020) which can be partially inferred by the *AE* index. Figure 4 shows that the occurrence rate of EMIC waves increases with *AE* values for all geomagnetic conditions. Occurrence rates at storm and quiet times are comparable for different *AE* bins. Quiet time EMIC occurrence rates at higher *AE* bins could be related to isolated non-storm time substorms (Remya et al., 2018) or steady magnetospheric convection events. Peak storm

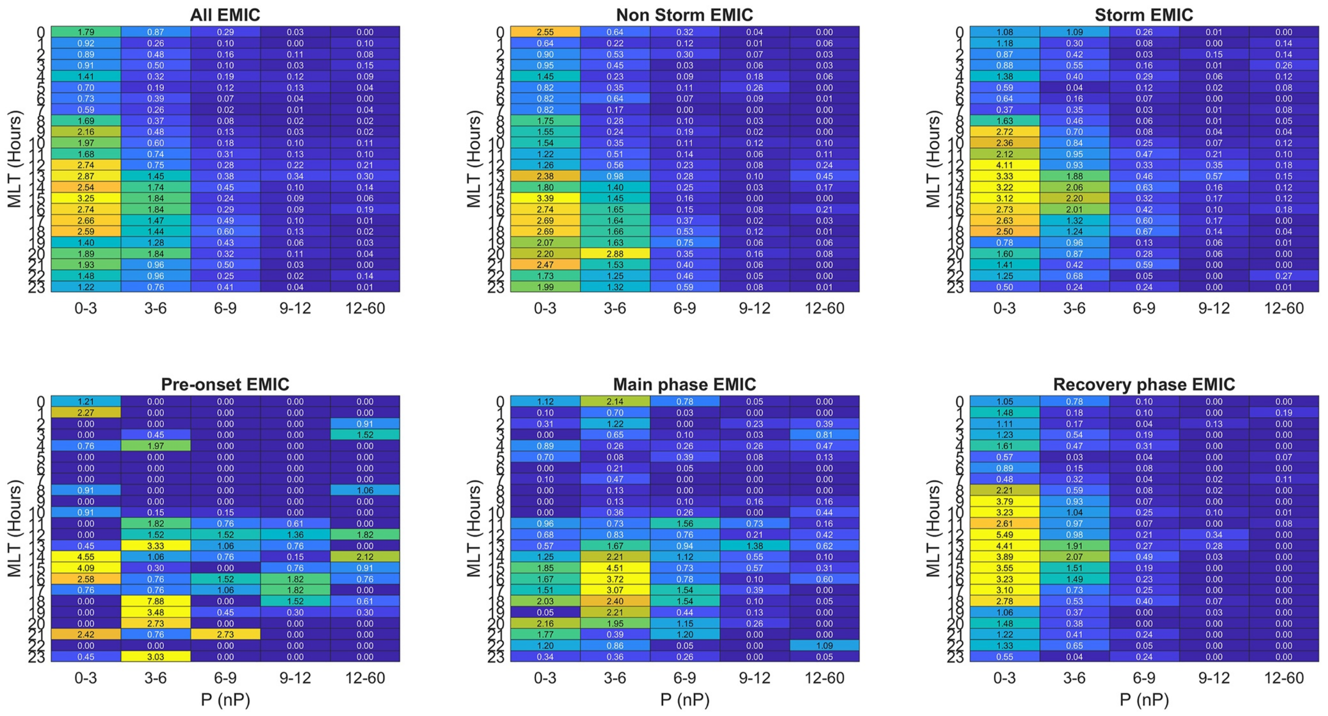

Figure 5. Heatmap of normalized EMIC wave occurrence rates for a given P_{dyn} and Magnetic Local Time bin during all times, non-storm and storm periods, and during the pre-onset, main, and recovery phases.

time occurrence rate is observed for pre-onset phase (22%), followed by main and recovery phases. The occurrence rates of EMIC waves for different *Kp* bins are illustrated in Figure S1 in Supporting Information S1. The occurrence rate peaks at $Kp = 4 - 6$ for non-storm time and pre-onset phases but otherwise exhibit an increasing trend with increasing *Kp* during storm time as well as during main and recovery phases.

As discussed above, Figure 3 suggests that dynamic pressure during both quiet and storm times plays an important role in the generation of EMIC waves. Enhancements in the solar wind dynamic pressure generate ion plasma anisotropies in the dayside magnetosphere which are capable of generating EMIC waves (Allen et al., 2013; Anderson & Hamilton, 1993; Engebretson et al., 2002; Lessard et al., 2019; Min et al., 2012; Olson & Lee, 1983; J.-S. Park et al., 2016; Saikin et al., 2015; Usanova et al., 2012). In order to understand the impact of solar wind dynamic pressure on the generation of EMIC waves during different geomagnetic conditions, we plot heatmaps showing EMIC occurrence rates in different P_{dyn} and MLT bins. Different panels in Figure 5 shows occurrence rates of EMIC waves in each bin of P_{dyn} and MLT, normalized to total number of EMIC waves observed under that geomagnetic condition. The color bar is not shown as the occurrence rate values are indicated in each bin. It can be seen that in general, all EMIC waves including the non-storm and storm time EMIC events have higher occurrence rates under low to medium pressure conditions with $P_{dyn} \leq 6$ nPa. Waves occurring under very low pressure ($P_{dyn} \leq 3$ nPa) conditions are more or less spread across at all MLT sectors with peak occurrence around post-noon to pre-midnight sectors and wave events with $3 < P_{dyn} \leq 6$ nPa peak in the post-noon sectors during all geomagnetic conditions. The quiet time EMIC events during low pressure conditions can be associated with the isolated substorm activities (Remya et al., 2018). Higher pressure bins with $P_{dyn} > 6$ nPa are predominantly observed during the pre-onset and main phases with peak occurrence spreading to morning and dawn sectors as pressure increases (see $P_{dyn} > 12$ nPa bins). The impact of solar wind dynamic pressure enhancements in the generation of EMIC waves is clearer when storm phases are considered, especially for the pre-onset conditions where majority of waves are generated by the dayside compression.

3.2. EMIC Wave Characteristics and Plasma Parameters

In the previous section we investigated the occurrence of EMIC waves as a function of quiet, storm phase, and solar wind/geomagnetic activity. In this section we investigate the spatial distribution of EMIC wave occurrence, wave amplitude, and background plasma characteristics.

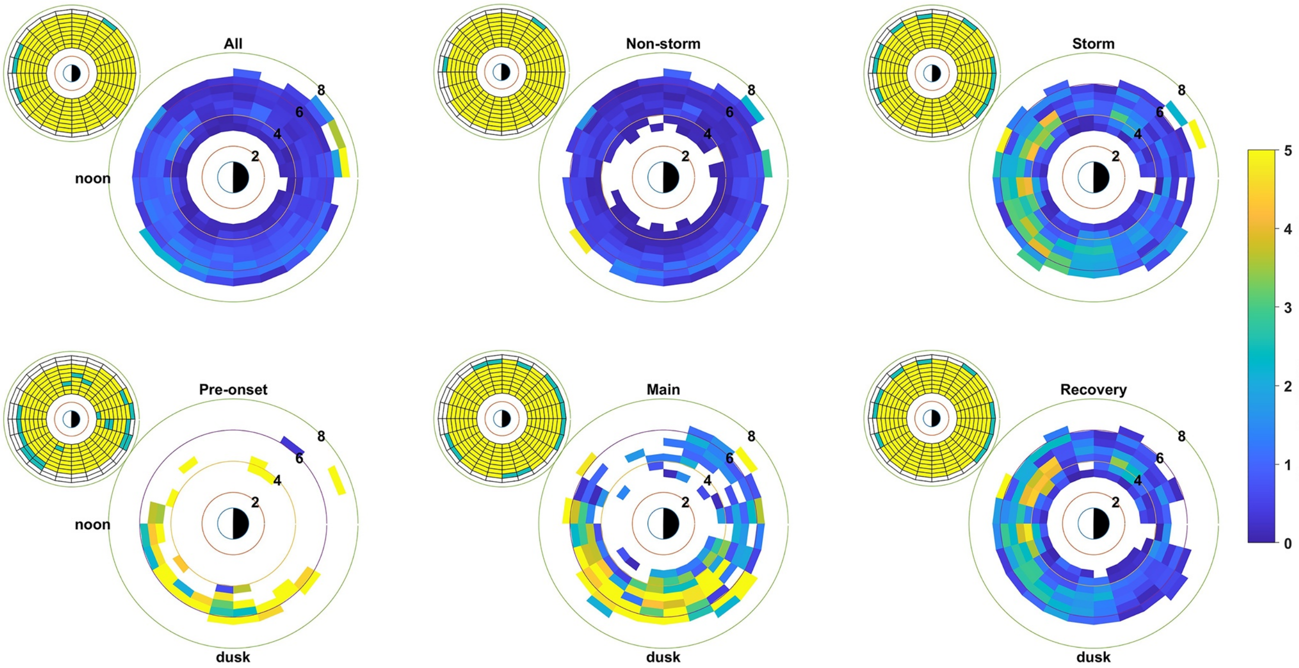

Figure 6. Polar plots of the EMIC wave occurrence rates during all time, non-storm and storm periods, and during the pre-onset, main, and recovery phases. The inlaid polar plots show a yellow when the satellite dwell time in the bin is statistically significant, blue when there is not enough dwell time, and white when it was not sampled.

3.2.1. EMIC Wave Occurrence

In order to accurately incorporate EMIC wave distribution and wave parameters into modeling efforts and understand when and how they influence the magnetospheric dynamics, it is important to quantify the occurrence of EMIC waves under varying geomagnetic conditions. Figure 6 illustrates the normalized EMIC wave occurrence rates during non-storm and storm times as well as during individual storm phases. The results are binned for 1 hr in MLT and 0.5 in L-shell. The inlaid plots in the panels show if the satellite had sufficient dwell time to be statistically valid (≥40 min of satellite dwell time) in a particular bin for a given magnetospheric condition. Yellow color shows statistically valid bins and blue if not. Majority of the bins had sufficient dwell time to be statistically valid. Statistically invalid bins are excluded from the study. The occurrence rates and satellite dwell time by bins during individual geomagnetic condition is given in Tables S1, S2, S9, S10, S17, S18, S25, S26, S33, and S24 in Supporting Information S1.

The normalized EMIC wave occurrence in Figure 6 for individual geomagnetic condition is obtained as the duration time of EMIC waves in each bin divided by the total dwell time of Van Allen Probes in that bin for a particular geomagnetic condition. The panels in Figure 6 clearly indicate that occurrence rates are higher during storm periods as compared to non-storm times in all L and MLT sectors. During geomagnetic storm a peak occurrence rate of ∼7% ($L = 7$, $MLT = 01$ hr) and a minimum of ∼0.02% ($L = 3$, $MLT = 07$ hr) were observed. The non-storm peak occurrence was ∼4.8% at $L = 6.5$, $MLT = 14$ hr and the minimum was ∼0.008% ($L = 3$, $MLT = 02$ hr). For the majority of the bins where EMIC waves were observed, storm time occurrence rates were higher at least by a factor of 2 than the non-storm time occurrence rates. The occurrence rates during storm time are found to be highest during the pre-onset phase with a maximum of ∼40.9% ($L = 7$, $MLT = 01$ hr) followed by recovery ∼12.5% ($L = 6$, $MLT = 10$ hr) and main phases ∼12.2% ($L = 6.5$, $MLT = 02$ hr) with almost equal peak values (Note that the color bars are chosen for uniformity and the occurrence rate values in each L-MLT bin is given in Tables S2, S10, S18, S26, and S34 in Supporting Information S1). However, even though the peak occurrence rates are nearly equal, the main phase occurrence rates are in general much higher as compared to recovery phase occurrence rates in various bins which is also evident from Figure 6. In fact, the second highest value in the recovery phase occurrence rate is ∼4.7% which is less than the top 20 values of occurrence rates for main phase bins. The minimum occurrence rates during the storm phases were ∼0.35% ($L = 6$, $MLT = 3$ hr), ∼0.13% ($L = 3$, $MLT = 15$ hr) and ∼0.03% ($L = 3$, $MLT = 7$ hr), respectively for pre-onset, main and recovery phases.

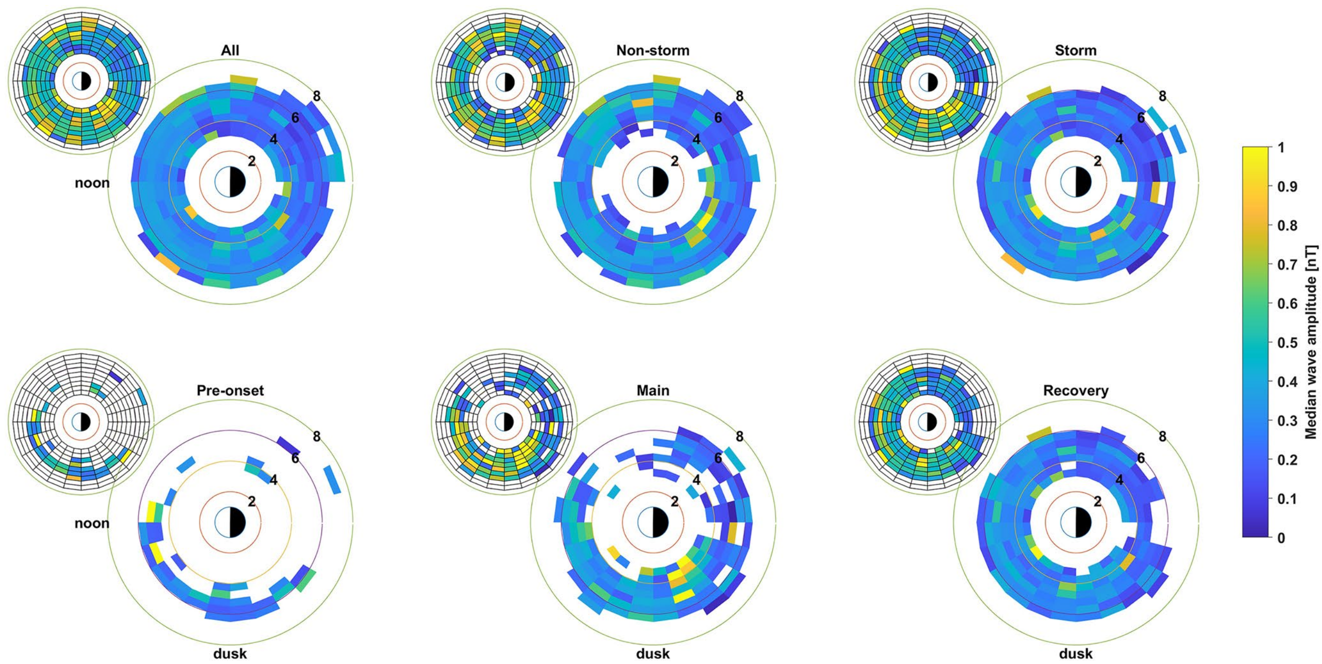

Figure 7. Polar plots of the median EMIC wave amplitude during all time, non-storm and storm periods, and during the pre-onset, main, and recovery phases. The inlaid plots show the upper quartiles of the EMIC wave amplitudes for each case.

The occurrence rates in the pre-onset phase are in general higher with a mean value of ∼7.5%, much higher than majority of the main and recovery phase bins.

Fewer waves are observed in the pre-onset phase as compared to other storm phases due to the 3 hr definition of the pre-onset period. In spite, the occurrence rates are very significant in all observed bins which dominated throughout the dayside and afternoon sectors indicating compression driven EMIC waves (Anderson & Hamilton, 1993; Engebretson et al., 2015; Usanova et al., 2008). The main phase occurrence rates in our study peaks from pre-noon to dusk sectors as expected and tend to increase at higher L and as one moves from dusk sector toward noon (Halford et al., 2016; Keika et al., 2013; Saikin et al., 2016; D. Wang et al., 2016). During the recovery phase, EMIC wave occurrence spreads to more MLT sectors with peak occurrence rates in the morning to noon (08–14 MLT), dusk (14–17 MLT) and dawn sectors (03–05 MLT) at lower L-shells. This could be due to the expanding plasmasphere which overlaps with the hot ion populations injected during the main phase thus exciting EMIC waves. It could also be that the existing particles and waves are drifted in those directions as the magnetosphere expands during the recovery phase. Though majority of the storm time EMIC wave events were observed in the recovery phase, the occurrence rates were fairly low during this period as compared to other phases, yet significantly higher than non-storm times.

3.2.2. EMIC Wave Amplitude

Figure 7 shows the distribution of median EMIC wave amplitudes during various geomagnetic conditions. In general, wave amplitudes are spread across all sectors uniformly and do not show preferential distribution over any L-MLT sectors. This is also true for the storm time where wave amplitudes are almost evenly distributed across all L/MLT bins and so were the wave amplitudes in the recovery phase. However, during pre-onset phase wave amplitudes show peaks in the noon sector and main phase shows amplitude peaks in the dusk/pre-midnight sectors, especially in the lower L-shells. EMIC waves observed during the non-storm intervals show peaks in wave amplitude in the dawn sector at $L > 5$ and in the pre-midnight sector at lower L-shells ($L < 5$). Maximum median wave amplitude of 2.62 nT was observed during the main phase at $L = 5$ and MLT = 19 hr. Typical EMIC wave amplitudes in different bins are found to be less than 1 nT as seen from Figure 7 with an average around 0.3 nT. However, peak wave amplitudes under different geomagnetic conditions are found to be quite higher.

EMIC wave amplitude is a key parameter in quantifying the impact that the waves have on energetic electrons within the outer radiation belt. To get an idea of how frequently the high amplitude waves occur and whether a quasi-linear or non-linear approach has to be incorporated to study these waves, we include polar plots of upper

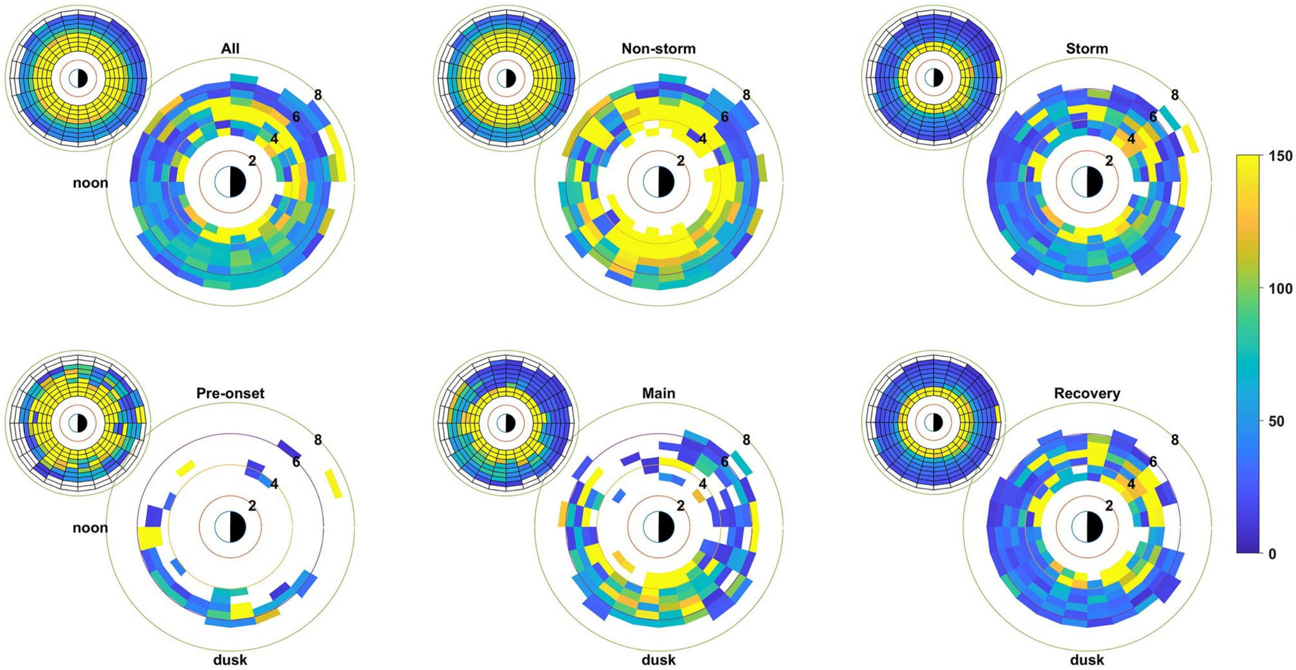

Figure 8. Polar plots of the median cold plasma density during all time, non-storm and storm periods, and during the pre-onset, main, and recovery phases. The inlaid polar plots show the median cold plasma number density when there were no EMIC waves observed for a given geomagnetic condition.

quartiles of the EMIC wave amplitudes as the inlaid plots in Figure 7. The upper quartile wave amplitudes in several bins were found close to or greater than 1 nT. Wave amplitudes with their upper quartile values above 1 nT range between 3% and 8% during different geomagnetic conditions. The peak amplitudes of these high amplitude waves range between 1 and 10 nT with ∼34% of the waves exceeding 2 nT during different geomagnetic conditions. Tables showing median wave amplitude and their upper and lower quartiles during different geomagnetic conditions is provided in Tables S3–S5, S11–S13, S19–S21, S27–S29, S35–S37 in Supporting Information S1.

3.2.3. EMIC Waves and Cold Plasma Density

The cold plasma can impact both the growth rates as well as the ability for EMIC waves to interact with ring current and radiation belt particles (Kozyra et al., 1984; Summers et al., 2007a, 2007b). Figure 8 illustrates polar plots of the median cold electron densities during EMIC waves for various L/MLT bins under different geomagnetic conditions. The inlaid polar plots show the median cold plasma density values when no EMIC waves are found. The cold plasma density for EMIC bins were found to be higher during quiet time (median ∼107 cm^{-3}) for $L < 5$ in the dusk and night/dawn sectors. During storm time, the median cold plasma density was ∼48 cm^{-3} with the highest median densities observed during the main phase (∼67 cm^{-3}). This was followed by pre-onset and recovery phases with almost equal median values (∼46 cm^{-3}). EMIC waves during storm time or storm phases do not show any associated dominant sector/s of increased cold plasma density. Tables showing median cold plasma number density and their upper and lower quarterlies during EMIC waves is provided in Tables S6–S8, S14–S16, S22–S24, S30–S32, S38–S40 in Supporting Information S1.

3.2.4. EMIC Waves and Local α^* Parameter

The local α^* parameter plays a role in determining the rate at which EMIC waves scatter the radiation belt electrons in to the loss cone it partly determines the minimum energy for EMIC wave/electron resonant interaction along with other parameters like properties of the EMIC wave spectrum and the local ion composition (Summers et al., 2007a; Summers & Thorne, 2003). The α^* parameter is defined as the magnetic energy per particle and is proportional to the square of Alfven speed (Summers et al., 2007a). The parameter α^* is given by the equation:

$$\alpha^* = \frac{\Omega_e^2}{\omega_{pe}^2} = \frac{V_A^2}{\epsilon c^2} = \frac{B_0^2}{4\pi N_0}\frac{1}{m_e c^2} \quad (1)$$

10.1029/2023JA031712

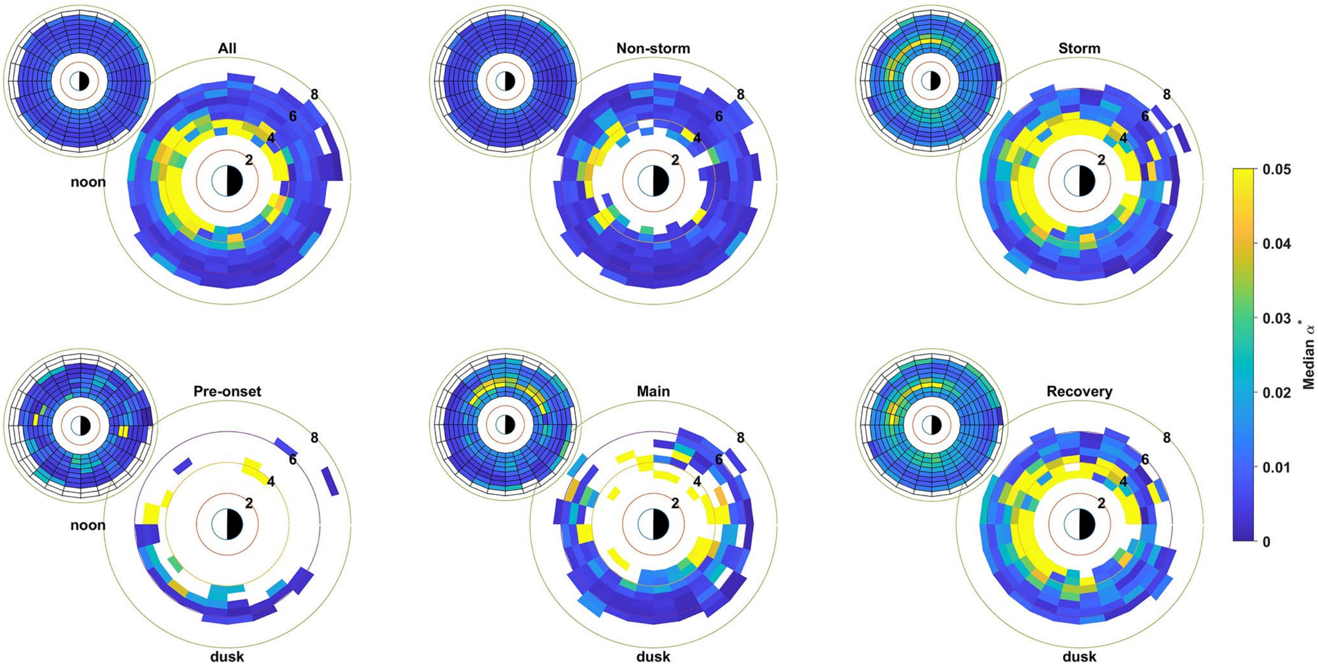

Figure 9. Polar plots of the median α^* during all time, non-storm and storm periods, and during the pre-onset, main, and recovery phases. The inlaid polar plots show α^* values when no EMIC waves were observed during a given geomagnetic condition.

where B_0 and N_0 are the background magnetic field and cold plasma density, respectively. A low value of the parameter α^*, typically $\alpha^* < 0.02$ is, found suitable for electron decay to occur (Summers & Thorne, 2003).

Figure 9 shows the polar plot of the local α^* parameter during EMIC waves and the inlaid plots show median α^* values when there are no EMIC waves. As α^* is proportional to the square of the magnetic field and inversely proportional to the cold plasma density, it is expected that the local α^* parameter will be low during EMIC waves as compared to when there are no EMIC waves observed. However, we do not observe any such clear indication. In general, the α^* values observed during quiet geomagnetic conditions (median $\alpha^* = 0.0046$) are lower than those found during geomagnetic storms (median $\alpha^* = 0.015$). The presence of plasmaspheric bulge in the dusk sector is evident from the low α^* values in this sector, especially from the non-storm, pre-onset and main phase panels. We find that lower L-shells have higher values of α^* during EMIC wave activity as compared to when no EMIC waves are observed.

4. Discussion and Comparison to Previous Studies

Using observations from Van Allen Probes measurements during September 2012 to July 2019 (approximately ~82 months), we examine the spatial occurrence and wave parameter distribution of EMIC waves with respect to geomagnetic storm phases during solar cycle 24 (maximum smoothed sunspot number 116.4). We identify a total of 144 geomagnetic storms which amounted to ~27% of storm time interval. Out of these, EMIC waves were found to be present during 131 of 144 (91%) identified storms. Statistical results in this study are demonstrated in such a way that they can be easily compared with similar previous studies where storm phase statistics are discussed (e.g., CRRES mission (Halford et al., 2016)). CRRES was operational during a very active solar cycle with a maximum smoothed sunspot number of 212.5. Moreover, the later part of the mission coincides with the downward slope of the solar maximum with its apogee moved to dusk sector where majority of storm time EMIC waves are known to occur. However, CRRES's apogee only covered 08–14 MLT (through midnight) when the mission ceased to function in October 1991. A predecessor to Van Allen Probes with similar orbit and onboard instrumentation, CRRES provides an excellent storm time statistics of EMIC waves for a comparative study, even with a shorter total coverage period. As CRRES did not sufficiently cover dayside and noon sectors (08–14 MLT) during its lifetime, Halford et al. (2016) suppose that most dayside compression generated wave events might be missed in their statistics. Additionally, we will compare our results with Erlandson and Ukhorskiy (2001),

10.1029/2023JA031712

D. Wang et al. (2016), Saikin et al. (2016), and other statistical studies. Erlandson and Ukhorskiy (2001) uses ~10 years of Dynamic Explorer 1 (DE 1) observations which was also operational during solar cycle 22 as was CRRES. In D. Wang et al. (2016) and Saikin et al. (2016), the authors have used data from Van Allen Probes during the period September 2012 to April 2014, when it finished its first precession of all MLT sectors.

4.1. Storm Definition and EMIC Wave Detection Methods

Storm time statistical studies using a larger database have been possible in the recent past due to more extensive in-situ measurements in the magnetosphere. Table 1 displays a brief summary of results from some of such past storm time EMIC wave statistics. These missions provide varied information on the storm time dynamics depending on the mission period (solar activity), satellite orbit (polar/equatorial, etc.) and mission coverage in L-MLT sectors. It is important to note that differences in methodologies used can lead to different quantitative results and hence the conclusions. For example, in this study and several other previous studies compared here, a 3 hr interval prior to the onset is defined as the pre-onset interval. However, we notice that many storms do not begin with an abrupt increase in the P_{dyn} or a SI, rather the solar wind dynamic pressure slowly builds up on the dayside magnetosphere few hours before a storm onset. This is generally observed for a CIR driven storm. However, for several CME driven storms identified during our study period, we observed multiple pressure pulses/sudden impulses which extend for several hours (~10–20 hr) before the onset of the storm (e.g., 2012/10/07-16, 2015/11/03-14 storm). We observed that there are EMIC waves generated throughout this compression period. However, due to the 3-hr definition for the pre-onset duration, these waves do not fall under the pre-onset period or, in general, under storm time EMIC even though their generation mechanism is the storm related compression of the dayside magnetosphere. On the other hand, study by Fraser et al. (2010) uses 3 days prior to the onset as the pre-storm period. However, this definition will overestimate the pre-storm period and hence the EMIC waves thus generated.

The number of EMIC waves, wave duration etc. depends on the criteria used to identify EMIC events in individual studies. Each criteria has its own limitations. For example, one drawback in our algorithm is about the identification of the start and end times of EMIC wave activity and hence the wave duration. Many times a satellite observes weaker amplitude at the beginning and enters into a stronger amplitude wave regime. So the time series data and hence the spectrogram will show weaker amplitude at the beginning of the wave which may not be detected in our algorithm if it doesn't meet the criteria of wave power >1 order of background intensity. Hence the start time or the wave onset time identified by our algorithm would be a later time when stronger wave activity starts. This applies for the end time as well. Hence the wave duration for such events are underestimated. We should note that for any spacecraft measurement, the actual wave onset time will be ambiguous due to the fact that we cannot know if the spacecraft entered into an already existing wave regime or if the waves were excited at that particular space and time when it is observed. Similarly, our wave selection criteria have missed out some of the events with spectral widths $\delta f < 0.1$ Hz, which is the second drawback in our wave detection method (see Figure 2). A comparative study based on the criteria used to identify EMIC events across different missions can be a subsequent study to apprehend the pros and cons of individual methods and adopt the most competent method for future analysis.

The significance of EMIC waves and its impact on the particle dynamics globally in the Earth's magnetosphere depends on the spatial and temporal extent of the wave generation region, the wave amplitude, and the duration of the wave activity. For Van Allen Probes, with geo-transfer like orbits, if a wave event is temporally sustained but spatially localized, it will only be observed as a few minutes of wave activity as the satellite will cross the same L and MLT next in ~9 hr (orbit period). Unless the waves last for more than ~9 hr (which is not always the case) or if we have multi-probe measurements with slightly different orbit periods, it will be hard to account for the effect of long lasting EMIC wave activity as possible cause for storm time particle losses. It is also to be noted that with single point measurements a significant amount of wave activity can be missed during any particular storm. The ambiguity of the wave onset and end time, and therefore the wave duration can be addressed efficiently with multi-probe measurements which will also be helpful in understanding the spatial and temporal evolution of the waves in the Earth's magnetosphere.

4.2. Geomagnetic Storms During Van Allen Probes Era

Table 2 shows a thorough comparison of storm periods identified in this study with results from some of the past statistical studies where storm phase dependence of EMIC waves are reported. In spite of our much longer

Table 1
Comparison of EMIC Wave Statistical Studies by Storm Phases

Study	Spacecraft	L-shell	MLT	Index	Key results
Kasahara et al. (1992)	Akebono	1–3	0–22, 23–24	*Kp*	Higher Kp values yield higher occurrence rates
Erlandson and Ukhorskiy (2001)	DE 1	3.5–5	All	*Dst*	(i) Normalized EMIC wave occurrence rate is ∼5 times higher during storm time than quiet time intervals (ii) Afternoon to premidnight sector have larger peak spectral density
Halford et al. (2016)	CRRES	3–8	14–24, 0–8	*Sym-H*	(i)Normalized EMIC wave occurrence rate ∼1.6 times higher during storm time than quiet time (ii) Majority of storm time EMIC waves in main phase; Highest occurrence rate also in main phase (iii) Uniform distribution of wave amplitudes across different geomagnetic conditions and across all MLTs
Fraser et al. (2010)	GOES	6.6	All	*Dst*	(i) Main phase waves were observed mostly in the He+ band (ii) CME generated storms have higher average wave spectral density during the main phase compared to CIR storms (iii) Wave amplitudes similar in prestorm, main and recovery phases
D. Wang et al. (2016)	Van Allen Probes	3–6	All	*Sym-H*	(i)Normalized EMIC wave occurrence rate is ∼2.8 times higher during storm time than quiet time intervals
Saikin et al. (2016)	Van Allen Probes	2–8	All	*Sym-H*	(i) Nonstorm EMIC waves predominant in prenoon and main and recovery phase in the afternoon sectors (ii) Low (high) pressure yield higher prenoon (dayside) occurrence rates
Present work	Van Allen Probes	3–7	All	*Sym-H*	(i)Normalized EMIC wave occurrence rate ∼2.9 times higher during storm time than quiet time (ii) Majority of storm time EMIC waves in recovery phase; Highest occurrence rate in pre-onset followed by main phase (iii) Main phase EMIC waves observed in the afternoon-pre-midnight sectors; Recovery phase waves in morning sector (iv) Wave amplitudes distribute uniformly across all geomagnetic conditions in almost all MLT sectors

study duration, Halford et al. (2016) had proportionally more storms (∼31%) during their study period. A major reason for higher storm number and duration during CRRES mission is because CRRES was operational during 1990–1991, the early descending phase of a very active solar cycle which peaked in 1989. The magnitude and number of geomagnetic storms is highest during descending phase of a solar cycle, two to three years after its peak (Gonzalez et al., 1990; Le et al., 2013), as it was during the CRRES period. Van Allen Probes was operational

Table 2
Comparison of Storm Periods Investigated by Previous Statistical Studies With Those in the Current Paper

Mission	Study period	# Of geomagnetic storms	% Of storm time	# Of storms with *Sym-H* < −150 nT	# Of storms with observed EMIC waves
Van Allen Probes A and B (present work)	September 2012 to July 2019 (~6.8 years)	144	~27%	4	131 (~91%)
Van Allen Probes A (D. Wang et al., 2016)	September 2012 to April 2014 (20 months)	76	~18%	0	50 (66%)
Van Allen Probes A and B (Saikin et al., 2016)	September 2012 to June 2014 (22 months)	73	~12%	NA	NA
CRRES (Halford et al., 2010; Halford et al., 2016)	July 1990 to October 1991 (15 months)	119	~31%	9	49 (41%)

during solar cycle 24 which was a very weak cycle in the recent history, weakest one since cycle 14 (1902–1913). The lower solar activity also led to low geomagnetic activity in this cycle and hence number of storms in the cycle were less as compared to previous cycles. It is also to be noted that Halford et al. (2010) used *Sym-H* < −40 nT criteria for determining storm times, unlike the present study where we use *Sym-H* < −50 nT criteria. At the same time (Erlandson & Ukhorskiy, 2001) uses a much stricter criteria of *Dst* ≤ −100 nT for defining storm periods. The definition of recovery phase is also different in all the above studies. Although D. Wang et al. (2016) and Saikin et al. (2016) used first precession of Van Allen Probes data, the storm time dwell time in the afternoon and early morning sectors in their study was significantly less compared to morning and dusk sectors (see Figure 4 of Saikin et al. (2016)). Nonetheless, with the larger data set in this study, we are able to cover longer duration of the solar cycle. This includes larger number of minor and major storms and the EMIC waves thus generated.

The average length of the storms in our study is 112.5 hr with mean lengths of main and recovery phases as 19 and 90.5 hr, respectively which are quite high as compared to Halford et al. (2016) with mean storm length of 28 hr and main and recovery phase length of 8 and 17.5 hr, respectively. The large difference in the lengths of storm and storm phases can be attributed to two main reasons. First, the lengths of recovery phases are affected by the difference in the geomagnetic activity level during these missions. Van Allen Probes era witnessed a mix of CME and CIR driven geomagnetic storms (Murphy et al., 2018) whereas CRRES era likely had more CME driven storms. There were no or very few consistent solar wind monitors during the CRRES era and hence we cannot categorize the storms from this period, however, CIR storms are generally observed during the declining phase of solar cycle (Hutchinson et al., 2011) and CRRES was operational during the peak of a very active solar cycle. CME driven storms are more intense and shorter in duration than CIR storms which explains the shorter lengths of storms during CRRES as compared to our study. Moreover, CME driven geomagnetic storms during low active solar cycle is caused by relatively slow CME which generally have longer main and recovery phases (Watari, 2017). As shown in Figure 6 of D. Wang et al. (2016), the storms during the CRRES mission recovered faster and had shorter recovery phases as compared to the ones during Van Allen Probes era. Second, it is strongly decided by the definition of the storm recovery. In Halford et al. (2016) the end of the recovery phase is defined as 80% recovery of the minimum *Sym-H* value. However, in this study, we define the end of recovery phase as the recovery of both the solar wind drivers and the *Dst* index and hence is longer as compared to Halford et al. (2016).

Table 3
Comparison of EMIC Wave Occurrences From Different Studies

			% Of storm time EMIC waves in each phase		
Mission	Non-storm	Storm	Pre-onset	Main	Recovery
Van Allen Probes (A and B) (present work)	48.2%	51.8%	4%	24.7%	71.9%
Van Allen Probes A (D. Wang et al., 2016)	54%	46%	8%	28%	64%
Van Allen Probes (A and B) (Saikin et al., 2016)	56%	44%	8.3%	27.4%	64.3%
CRRES (Halford et al., 2016)	42.9%	57.1%	5.6%	55.2%	39.2%
CRRES (Halford et al., 2010)	57.6%	42.4%	7.7%	56.3%	36.1%
DE 1[a] (Erlandson & Ukhorskiy, 2001)	80.6%	19.4%	8.7%	30.4%	60.9%

[a]Storm phase statistics calculated from the available information in their paper.

10.1029/2023JA031712

Atmospheric Losses of radiation belt relativistic electrons are determined to be more effective during storms with extended recovery phases than with fast recovery phases (Sandanger et al., 2009). Storm time statistics using the Van Allen Probes data can hence provide better understanding of the radiation belt loss processes. The lower solar activity also led to weaker geomagnetic storms (fewer intense storms) in our study period as compared to the CRRES duration. Hence it is important to consider the strength of the solar cycle while comparing different storm time statistics of EMIC waves from different missions.

4.3. Storm and Non-Storm Time EMIC Waves

In the present study, EMIC waves were found to be present during 131 of 144 (91%) storms as compared to 50 of 76 (66%) storms in D. Wang et al. (2016) and 49 of 119 (41%) storms in Halford et al. (2010, 2016).

The EMIC wave occurrence rates reported in the present study is 2.9 times more often during storm time intervals than during quiet period. This value is comparable to that from D. Wang et al. (2016) which is 2.8, but falls in between the values 1.6, reported from CRRES observations (Halford et al., 2010), and 5, reported from Dynamic Explorer 1 (DE 1) (Erlandson & Ukhorskiy, 2001). Interestingly, DE 1 and CRRES were both operational during solar cycle 22. While CRRES covered less than a year in its orbit, DE 1 results are from 10 years of data but looked only at intense ($Dst < -100$ nT) storms, which probably resulted in higher storm time occurrence ratio. It may also be noted that DE 1 was a polar orbiting satellite whereas CRRES and Van Allen Probes were equatorial missions, covering slightly different L-shells.

Out of the total 2,442 EMIC events (30,020 min) identified during our study period, storm time activity accounted for 15,548 min (∼52%) and remaining ∼48% during quiet times. A comparison of occurrence percentage of storm and quiet time EMIC waves and its storm phase occurrences from different missions is tabulated in Table 3. All the past and present studies are in concurrence that the normalized EMIC occurrence rates are higher during storm time than during quiet time.

In our study, recovery phase observed majority (11,174 min = 71.9%) of storm time EMIC wave activity while main and pre-onset phases respectively had ∼24.7% (3,840 min) and ∼4% (660 min) of recorded EMIC wave activity. The readers may kindly note that the duration of EMIC events in individual storm phases in our study (660 + 3,840 + 11,174=) is 15,674 min which is higher than our actual storm time duration of 15,548 min. This is because, as we are considering double/multi-dip storms as separate storm events, there is a 3 hr overlap of the recovery and the pre-onset phases of the adjacent storms which observe double/multi-dips in the *Sym-H*. Hence any EMIC wave occurring in this 3 hr overlap interval will be double counted. We found that there was a total of 126 min of EMIC wave activity in this overlapping interval.

4.4. EMIC Waves and Geomagnetic Indices

The occurrence rates for a given *Sym-H* bin in different storm phases are different. For example, the occurrence rate in the 40–50 nT *Sym-H* bin is 10.8% and 1.8% during pre-onset and main phases respectively, whereas the recovery phase occurrence rate is 0 for the same *Sym-H* bin. As the local ion plasma conditions like temperature, temperature anisotropy, composition, densities, etc., during the different storm phases vary even for the same value of geomagnetic index, considering storm phases can capture EMIC wave occurrence better than just a specific value of a geomagnetic index.

It is very interesting to note the discrepancy between the occurrence rates of EMIC waves versus *Sym-H* figures in this study (Figure 3) and that from CRRES (Figure 2 of Halford et al. (2016)). First of all, Halford et al. (2016) reports nearly zero occurrence rate in the main phase for $Sym\text{-}H < -100$ nT while their recovery phase occurrence rates were noteworthy in these bins. They suggest this discrepancy is due to the ionospheric outflow of Oxygen in the ring current during the main phase which could damp the EMIC wave growth. Albeit, due to shorter life times of Oxygen, EMIC waves could still grow in the late recovery phases if *Sym-H* is still disturbed with sufficient anisotropies in the ion populations. On the contrary, we find significant occurrence rates (6%) for EMIC waves during the main phase for *Sym-H* bins as low as ∼−200 nT while recovery phase occurrence rates drops to zero below $Sym\text{-}H < -150$. It is to be noted that our study period observed only 4 storms with $Sym\text{-}H < -150$ nT (see Table 2) whereas CRRES mission observed 9 such intense storms. Nevertheless, as reported by Halford et al. (2016) (Figure 2), CRRES mission did not observe any EMIC waves during storms with $Sym\text{-}H < -200$ nT.

An occurrence peak at $-220 < Sym\text{-}H < -230$ nT bin during the storm time in Figure 3 is noteworthy. However, when divided into different storm phases, the number of observations in the bin was less to be considered as statistically valid (<40 min) and hence is neglected in the storm phase plots. Below $Sym\text{-}H < -200$ nT values, we don't have enough statistics. Longer study duration with large number of intense storms is required to be able to understand the wave generation and dynamics at $Sym\text{-}H < -150$ nT.

As with the geomagnetic indices, solar wind dynamic pressure is also used to study the EMIC wave occurrence as it plays an important role in generation of the dayside EMIC waves. Past studies suggest that quiet time EMIC waves are mostly generated due to the solar wind pressure pulses/enhancements (Allen et al., 2013; Anderson & Hamilton, 1993; Engebretson et al., 2002; Lessard et al., 2019; Min et al., 2012; Olson & Lee, 1983; J.-S. Park et al., 2016; Saikin et al., 2015; Usanova et al., 2012). We find that EMIC waves driven by higher solar wind dynamic pressure $P_{dyn} > 6$ nPa are more often observed during the pre-onset and main phase than during quiet/non-storm time conditions. As is understood, the pre-onset events are associated with an increase in the solar wind dynamic pressure and the compression of the magnetosphere continues into the main phase during a storm. Our study shows that EMIC waves occurring under low pressure ($P_{dyn} \leq 3$ nPa) conditions are more or less spread across at all MLT sectors with peak occurrence around post-noon to pre-midnight sectors. This is seen during both non-storm and storm intervals. The non-storm EMIC events occurring during very low pressure conditions are clearly associated with the isolated substorm injections which provides the necessary free energy for the dusk-side EMIC events to grow (Remya et al., 2018, 2020). Higher pressure events $3 < P_{dyn} \leq 6$ nPa peak in the post-noon sectors during all geomagnetic conditions. EMIC waves associated with very high pressure solar wind conditions ($P_{dyn} > 6$ nPa) are observed mainly during the pre-onset and main phases with peak occurrence spreading to morning and dawn sectors with increase in P_{dyn}. This is different from the results obtained by Saikin et al. (2016) where the low pressure ($P_{dyn} < 3$ nPa) associated EMIC waves had higher occurrence rates in the pre-noon sector while the high pressure ($P_{dyn} \geq 3$ nPa) associated events were found to be more spread in MLTs. The difference in the results are because we consider the P_{dyn} effect during individual geomagnetic conditions while Saikin et al. (2016) consider only the effect of P_{dyn} and do not differentiate between non-storm, storm or storm phases.

It is evident that regardless of the geomagnetic activity index or solar wind parameters (e.g., P_{dyn}), individual storm phases show a clear impact on the EMIC wave occurrence and demonstrates the occurrence rates of EMIC waves better in comparison to using a single value (or range) of the geomagnetic index or solar wind dynamic pressure. As mentioned earlier, this is due to the greatly varying local plasma conditions during different storm phases. Here we also like to emphasize that wave and particle dynamics are contemporaneous and must be studied concurrently to completely understand the wave growth and decay processes during various geomagnetic conditions.

4.5. Wave Occurrence and Distribution

Several statistical studies using various satellite missions in the past report the occurrence pattern and spatial distribution of EMIC waves in the Earth's magnetosphere (Allen et al., 2015; Anderson et al., 1992; Erlandson & Ukhorskiy, 2001; Halford et al., 2010; Kasahara et al., 1992; Keika et al., 2013; Min et al., 2012; Saikin et al., 2015; Usanova et al., 2012; D. Wang et al., 2015; X. Y. Wang et al., 2017; Yu et al., 2015). Many among these studies examined the dependence of EMIC wave occurrence on geomagnetic activity and solar wind pressure using *AE*, *Kp*, *Dst*/*Sym-H* indices and P_{dyn}. Saikin et al. (2016) provides a list of such statistical studies covering ~30 years, solar cycles 21 through 24 (Table 4 in their paper). Storm time and especially storm phase statistics have been studied in the recent past by a very few among these Erlandson and Ukhorskiy (2001), Keika et al. (2013), Saikin et al. (2016), Halford et al. (2016), and D. Wang et al. (2016). In general, all storm time EMIC studies, including the current results, consistently show that the occurrence rates of EMIC waves are higher during the storm time as compared to quiet/non-storm time. This substantiates the understanding that these waves are more likely to occur during disturbed geomagnetic conditions.

The distribution of the EMIC waves during different storm phases are well corroborated with all past EMIC wave studies. Past and present studies show peak EMIC wave occurrence rates in the afternoon/dusk sectors during the storm main and recovery phases (negative *Sym-H*), in the noon and morning sectors during storm pre-onset (positive *Sym-H*) and in the morning and dawn sectors with more or less uniform coverage over all MLTs during non-storm time. Again, the main phase EMIC waves are predominantly seen to occur at noon to dusk sectors and at higher L-shells whereas the waves in the recovery phase are more or less uniformly distributed across all MLT sectors with a slightly higher predominance in the dayside. This scenario is consistent with the present understanding of EMIC wave generation mechanisms and the inner magnetosphere dynamics (Halford et al., 2010; Keika et al., 2013; Meredith et al., 2014; Saikin et al., 2016; Usanova et al., 2012; D. Wang et al., 2016). During the main phase, it is thought that the injection of ions from the tail contribute to an increase in temperature anisotropy which can help grow EMIC waves. During the recovery phase, the lingering temperature anisotropy, changes in the ion composition and background plasma may lead to EMIC wave generation at more MLT sectors as the ions will have had sufficient time to complete multiple drift paths. The studies using THEMIS and AMPTE/CCE, covering higher L-shells ($L > 6$), show a general predominance of EMIC waves in the afternoon sector although their overall occurrence rates are much higher compared to the lower L-shells.

Results from Freja (Bräysy et al., 1998), GOES (Fraser et al., 2010), and CRRES (Halford et al., 2010) show that the majority of the storm time EMIC waves were observed during the main phase whereas few other studies from GOES (Fraser et al., 2010), and Van Allen Probes (Saikin et al., 2016; D. Wang et al., 2016) and the present study using an extensive data set indicate higher number of storm time EMIC waves during the recovery phase of storms. We attribute this to the lengths of the recovery phases which in turn is associated with the storm drivers as discussed in Section 4.2. The recovery phases during the Van Allen Probe era were consistently longer as compared to those in the solar cycle 22 and hence have yielded higher number of recovery phase waves. On the other hand, the storm time occurrence rates in our study are found to be highest during the pre-onset phase (maximum ∼41%) which agrees with D. Wang et al. (2016). However, the authors mention lower dwell time in some of their pre-onset bins as well as very few number (10) of EMIC waves measured during their pre-onset period. The present study had sufficient observations and almost all the observed bins in the storm phases are statistically significant (see inlaid polar plots in Figure 6). CRRES results (Halford et al., 2016) have the maximum occurrence rates in their main phase followed by pre-onset and recovery phases. Due to the CRRES orbit not sufficiently sampling the 08–14 MLT in the dayside, which resulted in very few or no observations in these sectors, these results cannot be compared with the pre-onset peaks in our study. Regardless, all satellite studies consistently show that EMIC occurrence rates in different L-MLT sectors are significantly higher during the main phase of storm as compared to the recovery phase.

The occurrence rates in different bins during main and recovery phases in the present study remarkably differ from each other with main phase rates in the majority of the bins approximately twice as compared to the corresponding recovery rates. This is contrary to the results from the first precession of Van Allen Probes (D. Wang et al., 2016). Similarly, the pre-onset bins in our study often had much higher occurrence rates as compared to corresponding main or recovery phase bins. We observe a gap in occurrence of EMIC waves in the midnight sector (23-01 MLT) in the recovery phase as was also reported by D. Wang et al. (2016) around 22 MLT which could be attributed to the absence/decrease of the injected energetic ions.

The EMIC occurrence rates behave differently for different frequency bands during various geomagnetic conditions. Past statistical studies like Keika et al. (2013), Saikin et al. (2015), and a more recent study by Jun et al. (2021) show that the H^+ band EMIC waves have two major occurrence peaks. The morning (03–08MLT) sector peak is observed in the outer magnetosphere ($L > 8$) during quiet geomagnetic conditions. An occurrence peak in the noon sector (10–14MLT) is observed at lower L-shells ($L = 4$–6) during the recovery phase of a geomagnetic storm. These are attributed to the moderate magnetospheric compressions during the recovery of a storm. The He^+ band waves are also observed in same sector during recovery phase at comparatively lower L-shells (inside plasmasphere). The He^+ band waves have a strong occurrence peak in the dusk-midnight sector during the main phase of the storm at $L = 6$–8. Quiet time occurrence peak for He^+ band is observed in the dusk sector (17–21MLT) for higher L-shells ($L > 8$). A band separated statistics using the current database is not included in the present study.

4.6. Wave Amplitude

In general, the amplitude distribution of EMIC waves in our study is uniform across all MLT sectors as well as across all geomagnetic conditions. However, minor peaks in wave amplitudes are observed during the non-storm time in the pre-midnight sector in lower L-shells ($L < 5$). Storm time wave amplitudes are also more or less evenly distributed across all L/MLT bins and so were the wave amplitudes in the recovery phase. However, during pre-onset and main phases, wave amplitudes show peaks in the noon and the dusk/evening sectors ($L < 5$),

10.1029/2023JA031712

respectively. The dayside waves during pre-onset phase are the ones generated by magnetospheric compressions owing to solar wind dynamic pressure enhancements. The dusk/evening side waves during storms are due to the injection of ring current ions and those during non-storm intervals can be ascribed to isolated non-storm time substorm injections (Remya et al., 2018). Ion injections during isolated substorms are found to be associated with enhanced convection periods which can push the ions deeper and faster and provide the necessary free energy for the dusk side EMIC waves to grow (Remya et al., 2020). It is also evident from Figure 2 that non-storm time EMIC waves have higher occurrence with increasing AE index, an indicator of substorm activity. The dusk/evening sector EMIC waves found during the main phase are understood be the He^+ band waves which are known to have comparatively higher amplitudes (Meredith et al., 2014; Saikin et al., 2015). Similarly, the larger amplitude waves observed during the pre-onset due to sudden impulses are understood to be mainly H^+ band waves which are known to have large amplitudes in the dayside/noon sector (Anderson & Hamilton, 1993; Engebretson et al., 2015).

Amplitude distribution in this study is in agreement with the CRRES results (Halford et al., 2016) where no clear variation in the wave amplitudes were seen across different geomagnetic conditions. Typical EMIC wave amplitudes in different bins in are found to be less than 1 nT with an average around 0.3 nT which is also in agreement with CRRES results. As majority of the EMIC wave amplitudes were found below <1 nT we corroborate quasi-linear assumption for EMIC waves in modeling studies. Nevertheless, non-linear effects need to be taken in to account at times for studying the large amplitude (≫1 nT) EMIC waves.

4.7. Cold Plasma Density and Local α^* Parameter

The cold plasma density for EMIC bins were higher during quiet times at low L-shells and in the dusk, night, and dawn sectors. (Halford et al., 2016) reports that during the CRRES mission cold plasma densities observed during EMIC waves were on an average 3 times larger than those when no EMIC waves were observed. In this study using Van Allen Probes measurements, we notice that during storm time and individual storm phases, the ratio of cold plasma densities in the bins with EMIC waves to those with no EMIC waves were found to be only ∼1.2%–1.5%. We concur that though higher cold plasma densities may help EMIC to have larger wave growths, high density regions do not necessarily favor EMIC wave occurrence (Fraser & Nguyen, 2001; Halford et al., 2015; Posch et al., 2010; Tetrick et al., 2017).

It is expected that the local α^* values will be low during EMIC waves as compared to when there are no EMIC waves as the α^* parameter is proportional to the square of the magnetic field and inversely proportional to the cold plasma density. However, our study do not show any clear evidence indicating so.

5. Summary and Conclusions

In this study, using measurements from Van Allen Probes A and B during the whole mission period from September 2012 to July 2019, we have performed a statistical analysis to establish the relation between geomagnetic storms and EMIC wave events in the Earth's magnetosphere. The analysis incorporates 2,442 EMIC wave events and 144 geomagnetic storms identified during this period to show their spatial distributions, occurrence rates, and several wave and plasma parameters with respect to non-storm time, storm time and during different storm phases. This survey serves as an extension to previous statistical studies of EMIC waves in the Earth's magnetosphere with special focus on the dependence of its occurrence and wave parameters on the storm phase dynamics. Results from our study are summarize as follows.

1. EMIC waves are found to occur 2.9 times more often during storm times as compared to non-storm times.
2. Occurrence rates of EMIC waves in L-MLT bins during different storm phases is found to be highest during the pre-onset phase with a peak of ∼40.9% followed by the recovery and main phases with almost equal peak values (∼12.5% and ∼12.2%, respectively). Nevertheless, main phase occurrence rates are in general found to be much higher in the majority of L-MLT bins as compared to the corresponding recovery phase occurrence rates.
3. Non-storm EMIC waves are spread uniformly across all MLT sectors. Main phase EMIC waves are dominant throughout the dusk and pre-midnight sectors whereas the recovery phase waves are more spread in MLT with peak around dawn to noon sector. The pre-onset waves are predominant in the noon to dusk sectors.
4. EMIC wave events occurring under low pressure (P_{dyn} ≤ 3 nPa) conditions during all geomagnetic conditions are spread across all MLT sectors with peak occurrence rates around post-noon sector. Events under

$3 < P_{dyn} \leq 6$ nPa also peak in the post-noon and pre-midnight sectors during all geomagnetic conditions. Storm phase analysis shows that EMIC wave events occurring at $P_{dyn} > 6$ nPa are predominantly observed during the pre-onset and main phases with peak occurrence spreading to morning and dawn sectors at higher pressure ($P_{dyn} > 12$ nPa) conditions.

5. Higher amplitude waves were predominantly found during non-storm conditions as much as during storm time and are found to prevail in the dusk to pre-midnight sectors.

In order to account for the ring current and radiation belt electron losses, which is believed to be strongly influenced by EMIC waves, it is very important to have larger statistics for EMIC waves during intense storms. The intense storms during Van Allen Probes and CRRES duration added together give less than 15 such storms (<−150 nT) which is not sufficient enough to carry out a statistical study. So it is important to have future missions in the inner magnetosphere with simultaneous wave and particle measurements. Since EMIC waves are highly localized in L and MLT, it is also important to have continuous measurements, especially with multi-probe missions, which would give us a better opportunity to look specifically for the wave impact on the storm time ring current loss processes.

The EMIC wave growth and amplification in a given region is controlled by various particle parameters like ion temperature anisotropy, parallel ion temperature, cold plasma density, ion composition, etc. and these parameters vary from one region to another even within the inner magnetosphere during different geomagnetic conditions. The wave occurrence studies hence need to be complemented with the particle data in order to be able to understand the local field and plasma conditions facilitating wave growth in that region. An in-depth analysis of particle measurements in coherence with the wave data will be a future work.

Data Availability Statement

Publicly available data sets were analyzed in this study. These data can be found here: Van Allen Probes ECT and EMFISIS from http://spdf.gsfc.nasa.gov/pub/data/rbsp/; Geomagnetic activity data from http://wdc.kugi.kyoto-u.ac.jp/kp/index.html; Solar wind parameters from https://spdf.gsfc.nasa.gov/pub/data/omni/. The list of geomagnetic storms used in this study is available at Zenodo via https://doi.org/10.5281/zenodo.8137913 (Remya et al., 2023).

Acknowledgments
We thank the Van Allen Probes ECT and EMFISIS teams and acknowledge the use of NASA/GSFC's Space Physics Data Facility's OMNI/CDAWeb for solar wind parameters and geomagnetic indices. KRM acknowledges support from NERC grants NE/P017185/2, NE/V002554/2 and STFC Grant ST/V006320/1. AJH and KRM were in part supported by the Space Precipitation Impacts project at Goddard Space Flight Center through the Heliophysics Internal Science Funding Model. The authors would like to acknowledge ISSI for the opportunity it offered for constructive team discussions on this topic as part of the International Team #522 led by RB and AJH.

References

Allen, R. C., Zhang, J. C., Kistler, L. M., Spence, H. E., Lin, R. L., Dunlop, M. W., & Andre, M. (2013). Multiple bidirectional EMIC waves observed by Cluster at middle magnetic latitudes in the dayside magnetosphere. *Journal of Geophysical Research: Space Physics*, *118*(10), 6266–6278. https://doi.org/10.1002/jgra.50600

Allen, R. C., Zhang, J.-C., Kistler, L. M., Spence, H. E., Lin, R.-L., Klecker, B., et al. (2015). A statistical study of EMIC waves observed by cluster: 1. Wave properties. *Journal of Geophysical Research: Space Physics*, *120*(7), 5574–5592. https://doi.org/10.1002/2015JA021333

Anderson, B. J., Erlandson, R. E., & Zanetti, L. J. (1992). A statistical study of Pc 1-2 magnetic pulsations in the equatorial magnetosphere: 1. Equatorial occurrence distributions. *Journal of Geophysical Research*, *97*(A3), 3075–3088. https://doi.org/10.1029/91JA02706

Anderson, B. J., & Hamilton, D. C. (1993). Electromagnetic ion cyclotron waves stimulated by modest magnetospheric compressions. *Journal of Geophysical Research*, *98*(A7), 11369–11382. https://doi.org/10.1029/93JA00605

Blake, J. B., Carranza, P. A., Claudepierre, S. G., Clemmons, J. H., Crain, W. R., Dotan, J., et al. (2013). The Magnetic Electron Ion Spectrometer (MagEIS) instruments aboard the radiation belt storm probes (RBSP) spacecraft. *Space Science Reviews*, *179*(1–4), 1–4. https://doi.org/10.1007/S11214-013-9991-8

Blum, L. W., Halford, A. J., Millan, R., Bonnell, J. W., Goldstein, J., Usanova, M., et al. (2015). Observations of coincident EMIC wave activity and duskside energetic electron precipitation on 18–19 January 2013. *Geophysical Research Letters*, *42*(14), 5727–5735. https://doi.org/10.1002/2015GL065245

Blum, L. W., Macdonald, E. A., Gary, S. P., Thomsen, M. F., & Spence, H. E. (2009). Ion observations from geosynchronous orbit as a proxy for ion cyclotron wave growth during storm times. *Journal of Geophysical Research*, *114*(A10), A10214. https://doi.org/10.1029/2009JA014396

Bortnik, J., Cutler, J. W., Dunson, C., & Bleier, T. E. (2007). An automatic wave detection algorithm applied to Pc1 pulsations. *Journal of Geophysical Research*, *112*(A4), A04204. https://doi.org/10.1029/2006JA011900

Bortnik, J., Cutler, J. W., Dunson, C., Bleier, T. E., & McPherron, R. L. (2008). Characteristics of low latitude Pc1 pulsations during geomagnetic storms. *Journal of Geophysical Research*, *113*(A4), A04201. https://doi.org/10.1029/2007JA012867

Bräysy, T., Mursula, K., & Marklund, G. (1998). Ion cyclotron waves during a great magnetic storm observed by Freja double-probe electric field instrument. *Journal of Geophysical Research*, *103*(A3), 4145–4155. https://doi.org/10.1029/97JA02820

Chen, H., Gao, X., Lu, Q., & Wang, S. (2019). Analyzing emic waves in the inner magnetosphere using long-term van Allen probes observations. *Journal of Geophysical Research: Space Physics*, *124*(9), 7402–7412. https://doi.org/10.1029/2019JA026965

Cornwall, J. M. (1965). Cyclotron instabilities and electromagnetic emission in the ultra low frequency and very low frequency ranges. *Journal of Geophysical Research*, *70*(1), 61–69. https://doi.org/10.1029/JZ070i001p00061

Cornwall, J. M., Coroniti, F. V., & Thorne, R. M. (1970). Turbulent loss of ring current protons. *Journal of Geophysical Research*, *75*(25), 4699–4709. https://doi.org/10.1029/JA075i025p04699

Davis, T. N., & Sugiura, M. (1966). Auroral electrojet activity index ae and its universal time variations. *Journal of Geophysical Research*, *71*(3), 785–801. https://doi.org/10.1029/jz071i003p00785

Engebretson, M. J., Lessard, M. R., Bortnik, J., Green, J. C., Horne, R. B., Detrick, D. L., et al. (2008). Pc1–Pc2 waves and energetic particle precipitation during and after magnetic storms: Superposed epoch analysis and case studies. *Journal of Geophysical Research*, *113*(A1). https://doi.org/10.1029/2007JA012362

Engebretson, M. J., Peterson, W. K., Posch, J. L., Klatt, M. R., Anderson, B. J., Russell, C. T., et al. (2002). Observations of two types of pc 1–2 pulsations in the outer dayside magnetosphere. *Journal of Geophysical Research*, *107*(A12), SMP20-1–SMP20-20. https://doi.org/10.1029/2001JA000198

Engebretson, M. J., Posch, J. L., Wygant, J. R., Kletzing, C. A., Lessard, M. R., Huang, C.-L., et al. (2015). Van Allen probes, NOAA, GOES, and ground observations of an intense EMIC wave event extending over 12 h in magnetic local time. *Journal of Geophysical Research: Space Physics*, *120*(7), 5465–5488. https://doi.org/10.1002/2015JA021227

Erlandson, R. E., & Ukhorskiy, A. J. (2001). Observations of electromagnetic ion cyclotron waves during geomagnetic storms: Wave occurrence and pitch angle scattering. *Journal of Geophysical Research*, *106*(A3), 3883–3895. https://doi.org/10.1029/2000JA000083

Fraser, B. J., Grew, R. S., Morley, S. K., Green, J. C., Singer, H. J., Loto'aniu, T. M., & Thomsen, M. F. (2010). Storm time observations of electromagnetic ion cyclotron waves at geosynchronous orbit: Goes results. *Journal of Geophysical Research*, *115*(A5). https://doi.org/10.1029/2009JA014516

Fraser, B. J., & Nguyen, T. S. (2001). Is the plasmapause a preferred source region of electromagnetic ion cyclotron waves in the magnetosphere? *Journal of Atmospheric and Solar-Terrestrial Physics*, *63*(11), 1225–1247. https://doi.org/10.1016/S1364-6826(00)00225-X

Gonzalez, W., Gonzalez, A., & Tsurutani, B. (1990). Dual-peak solar cycle distribution of intense geomagnetic storms. *Planetary and Space Science*, *38*(2), 181–187. https://doi.org/10.1016/0032-0633(90)90082-2

Halford, A. J., Fraser, B. J., & Morley, S. K. (2010). EMIC wave activity during geomagnetic storm and nonstorm periods: CRRES results. *Journal of Geophysical Research*, *115*(A12), A12248. https://doi.org/10.1029/2010JA015716

Halford, A. J., Fraser, B. J., & Morley, S. K. (2015). EMIC waves and plasmaspheric and plume density: CRRES results. *Journal of Geophysical Research: Space Physics*, *120*(3), 1974–1992. https://doi.org/10.1002/2014JA020338

Halford, A. J., Fraser, B. J., Morley, S. K., Elkington, S. R., & Chan, A. A. (2016). Dependence of EMIC wave parameters during quiet, geomagnetic storm, and geomagnetic storm phase times. *Journal of Geophysical Research: Space Physics*, *121*(7), 6277–6291. https://doi.org/10.1002/2016JA022694

Hutchinson, J. A., Wright, D. M., Milan, S. E., Grocott, A., & Boakes, P. D. (2011). A new way to study geomagnetic storms. *Astronomy and Geophysics*, *52*(4), 4.20–4.23. https://doi.org/10.1111/j.1468-4004.2011.52420.x

Jacobs, J. A., Kato, Y., Matsushita, S., & Troitskaya, V. A. (1964). Classification of geomagnetic micropulsations. *Journal of Geophysical Research*, *69*(1), 180–181. https://doi.org/10.1029/JZ069i001p00180

Jordanova, V., Farrugia, C., Thorne, R., Khazanov, G. V., Reeves, G., & Thomsen, M. (2001). Modeling ring current proton precipitation by EMIC waves during the May 14-16, 1997, storm. *Journal of Geophysical Research*, *106*(A1), 7–22. https://doi.org/10.1029/2000JA002008

Jun, C.-W., Miyoshi, Y., Kurita, S., Yue, C., Bortnik, J., Lyons, L., et al. (2021). The characteristics of emic waves in the magnetosphere based on the van Allen probes and Arase observations. *Journal of Geophysical Research: Space Physics*, *126*(6), e2020JA029001. https://doi.org/10.1029/2020JA029001

Kamide, Y., & Akasofu, S.-I. (1983). Notes on the auroral electrojet indices. *Review of Geophysics*, *21*(7), 1647–1656. https://doi.org/10.1029/rg021i007p01647

Kasahara, Y., Sawada, A., Yamamoto, M., Kimura, I., Kokubun, S., & Hayashi, K. (1992). Ion cyclotron emissions observed by the satellite Akebono in the vicinity of the magnetic equator. *Radio Science*, *27*(2), 347–362. https://doi.org/10.1029/91RS01872

Keika, K., Takahashi, K., Ukhorskiy, A. Y., & Miyoshi, Y. (2013). Global characteristics of electromagnetic ion cyclotron waves: Occurrence rate and its storm dependence. *Journal of Geophysical Research: Space Physics*, *118*(7), 4135–4150. https://doi.org/10.1002/jgra.50385

Kennel, C. F., & Petschek, H. E. (1966). Limit on stably trapped particle fluxes. *Journal of Geophysical Research*, *71*, 1–28. https://doi.org/10.1029/JZ071i001p00001

Khazanov, G. V., Gamayunov, K. V., Gallagher, D. L., & Kozyra, J. U. (2006). Self-consistent model of magnetospheric ring current and propagating electromagnetic ion cyclotron waves: Waves in multi-ion magnetosphere. *Journal of Geophysical Research*, *111*(A10), A10202. https://doi.org/10.1029/2006JA011833

Kletzing, C. A., Kurth, W. S., Acuna, M., MacDowall, R. J., Torbert, R. B., Averkamp, T., et al. (2013). The Electric and Magnetic Field Instrument Suite and Integrated Science (EMFISIS) on RBSP. *Space Science Reviews*, *179*(1–4), 127–181. https://doi.org/10.1007/s11214-013-9993-6

Kozyra, J. U., Cravens, T. E., Nagy, A. F., Fontheim, E. G., & Ong, R. S. B. (1984). Effects of energetic heavy ions on electromagnetic ion cyclotron wave generation in the plasmapause region. *Journal of Geophysical Research*, *89*(A4), 2217–2233. https://doi.org/10.1029/JA089iA04p02217

Le, G.-M., Cai, Z.-Y., Wang, H.-N., Yin, Z.-Q., & Li, P. (2013). Solar cycle distribution of major geomagnetic storms. *Research in Astronomy and Astrophysics*, *13*(6), 739–748. https://doi.org/10.1088/1674-4527/13/6/013

Lessard, M. R., Paulson, K., Spence, H. E., Weaver, C., Engebretson, M. J., Millan, R., et al. (2019). Generation of emic waves and effects on particle precipitation during a solar wind pressure intensification with bz>0. *Journal of Geophysical Research: Space Physics*, *124*(6), 4492–4508. https://doi.org/10.1029/2019JA026477

Li, W., Thorne, R., Angelopoulos, V., Bortnik, J., Cully, C. M., Ni, B., et al. (2009). Global distribution of whistler-mode chorus waves observed on the Themis spacecraft. *Geophysical Research Letters*, *36*(9), L09104. https://doi.org/10.1029/2009GL037595

Loto'aniu, T. M., Fraser, B. J., & Waters, C. L. (2005). Propagation of electromagnetic ion cyclotron wave energy in the magnetosphere. *Journal of Geophysical Research*, *110*(A7), A07214. https://doi.org/10.1029/2004JA010816

Mauk, B. H., Fox, N. J., Kanekal, S. G., Kessel, R. L., Sibeck, D. G., & Ukhorskiy, A. (2013). Science objectives and rationale for the radiation belt storm probes mission. *Space Science Reviews*, *179*(1–4), 3–27. https://doi.org/10.1007/s11214-012-9908-y

McCollough, J. P., Elkington, S. R., & Baker, D. N. (2012). The role of Shabansky orbits in compression-related electromagnetic ion cyclotron wave growth. *Journal of Geophysical Research*, *117*(A1), A01208. https://doi.org/10.1029/2011JA016948

Meredith, N. P., Horne, R. B., Kersten, T., Fraser, B. J., & Grew, R. S. (2014). Global morphology and spectral properties of EMIC waves derived from CRRES observations. *Journal of Geophysical Research: Space Physics*, *119*(7), 5328–5342. https://doi.org/10.1002/2014JA020064

Min, K., Lee, j., Keika, K., & Li, W. (2012). Global distribution of EMIC waves derived from THEMIS observations. *Journal of Geophysical Research*, *117*(A5), A05219. https://doi.org/10.1029/2012JA017515

Miyoshi, Y., Sakaguchi, K., Shiokawa, K., Evans, D., Albert, J., Connors, M., & Jordanova, V. (2008). Precipitation of radiation belt electrons by EMIC waves, observed from ground and space. *Geophysical Research Letters*, *35*(23), L23101. https://doi.org/10.1029/2008GL035727

Murphy, K. R., Forsyth, C. F., Reeves, G. D., Watt, C. E. J., Mann, I. R., Rae, I. J., et al. (2018). The global statistical response of the outer radiation belt during geomagnetic storms. *Geophysical Research Letters*, *45*(9), 3783–3792. https://doi.org/10.1002/2017GL076674

Olson, J. V., & Lee, L. C. (1983). Pc1 wave generation by sudden impulses. *Planetary and Space Science*, *31*(3), 295–297. https://doi.org/10.1016/0032-0633(83)90079-X

Park, J., Lühr, H., & Rauberg, J. (2013). Global characteristics of pc1 magnetic pulsations during solar cycle 23 deduced from champ data. *Annales Geophysicae*, *31*(9), 1507–1520. https://doi.org/10.5194/angeo-31-1507-2013

Park, J.-S., Kim, K.-H., Shiokawa, K., Lee, D.-H., Lee, E., Kwon, H.-J., et al. (2016). Emic waves observed at geosynchronous orbit under quiet geomagnetic conditions (kp ≤ 1). *Journal of Geophysical Research: Space Physics*, *121*(2), 1377–1390. https://doi.org/10.1002/2015JA021968

Posch, J. L., Engebretson, M. J., Murphy, M. T., Denton, M. H., Lessard, M. R., & Horne, R. B. (2010). Probing the relationship between electromagnetic ion cyclotron waves and plasmaspheric plumes near geosynchronous orbit. *Journal of Geophysical Research*, *115*(A11), A11205. https://doi.org/10.1029/2010JA015446

Rauch, J. L., & Roux, A. (1982). Ray tracing of ULF waves in a multicomponent magnetospheric plasma: Consequences for the generation mechanism of ion cyclotron waves. *Journal of Geophysical Research*, *87*(A10), 8191–8198. https://doi.org/10.1029/JA087iA10p08191

Remya, B., Halford, A., Sibeck, D., Murphy, K., & Fok, M.-C. (2023). *List of geomagnetic storms for the period September 2012 - July, 2019*. Zenodo. https://doi.org/10.5281/zenodo.8137913

Remya, B., Sibeck, D. G., Halford, A. J., Murphy, K. R., Reeves, G. D., Singer, H. J., et al. (2018). Ion injection triggered emic waves in the earth's magnetosphere. *Journal of Geophysical Research: Space Physics*, *123*(6), 4921–4938. https://doi.org/10.1029/2018JA025354

Remya, B., Sibeck, D. G., Ruohoniemi, J. M., Kunduri, B., Halford, A. J., Reeves, G. D., & Reddy, R. V. (2020). Association between emic wave occurrence and enhanced convection periods during ion injections. *Geophysical Research Letters*, *47*(3), e2019GL085676. https://doi.org/10.1029/2019GL085676

Rostoker, G. (1972). Geomagnetic indices. *Review of Geophysics*, *10*(4), 935–950. https://doi.org/10.1029/rg010i004p00935

Saikin, A. A., Zhang, J.-C., Allen, R. C., Smith, C. W., Kletzing, L. M. K. H. E. S. R. B. T. C. A., Jordanova, V. K., et al. (2015). The occurrence and wave properties of H^+-He^+-and O^+-band EMIC waves observed by the Van Allen Probes. *Journal of Geophysical Research: Space Physics*, *120*(9), 7477–7492. https://doi.org/10.1002/2015JA021358

Saikin, A. A., Zhang, J.-C., Smith, C. W., Spence, H. E., Torbert, R. B., & Kletzing, C. A. (2016). The dependence on geomagnetic conditions and solar wind dynamic pressure of the spatial distributions of EMIC waves observed by the Van Allen Probes. *Journal of Geophysical Research: Space Physics*, *121*(5), 4362–4377. https://doi.org/10.1002/2016JA022523

Sandanger, M., Søraas, F., Sørbø, M., Aarsnes, K., Oksavik, K., & Evans, D. (2009). Relativistic electron losses related to emic waves during CIR and CME storms. *Journal of Atmospheric and Solar-Terrestrial Physics*, *71*(10), 1126–1144. https://doi.org/10.1016/j.jastp.2008.07.006

Sckopke, N. (1966). A general relation between the energy of trapped particles and the disturbance field near the earth. *Journal of Geophysical Research*, *71*(13), 3125–3130. https://doi.org/10.1029/jz071i013p03125

Shabansky, V. P. (1971). Some processes in the magnetosphere. *Space Science Reviews*, *12*(3), 299–418. https://doi.org/10.1007/BF00165511

Shumko, M., Gallardo-Lacourt, B., Halford, A. J., Blum, L. W., Liang, J., Miyoshi, Y., et al. (2022). Proton aurora and relativistic electron microbursts scattered by electromagnetic ion cyclotron waves. *Frontiers in Astronomy and Space Sciences*, *9*. https://doi.org/10.3389/fspas.2022.975123

Spence, H., Reeves, G., Baker, D., Blake, J., Bolton, M., Bourdarie, S., et al. (2013). Science goals and overview of the radiation belt storm probes (RBSP) energetic particle, composition, and thermal plasma (ECT) suite on NASA's Van Allen probes mission. *Space Science Reviews*, *179*(1–4), 311–336. https://doi.org/10.1007/s11214-013-0007-5

Su, Z., Zhu, H., Xiao, F., Zheng, H., Shen, C., Wang, Y., & Wang, S. (2013). Latitudinal dependence of nonlinear interaction between electromagnetic ion cyclotron wave and radiation belt relativistic electrons. *Journal of Geophysical Research: Space Physics*, *118*(6), 3188–3202. https://doi.org/10.1002/jgra.50289

Sugiura, M. (1964). Hourly values of equatorial dst for the igy. *Annals of the International Geophysical Year*, *9*, 9–45.

Summers, D., Ni, B., & Meredith, N. P. (2007a). Timescale for radiation belt electron acceleration and loss due to resonant wave-particle interactions: 2. Evaluation for VLF chorus, ELF hiss, and electromagnetic ion cyclotron waves. *Journal of Geophysical Research*, *112*(A4), A04207. https://doi.org/10.1029/2006JA011993

Summers, D., Ni, B., & Meredith, N. P. (2007b). Timescales for radiation belt electron acceleration and loss due to resonant wave particle interactions: 1. Theory. *Journal of Geophysical Research*, *112*(A4), A04206. https://doi.org/10.1029/2006JA011801

Summers, D., & Thorne, R. M. (2003). Relativistic electron pitch-angle scattering by electromagnetic ion cyclotron waves during geomagnetic storms. *Journal of Geophysical Research*, *108*(A4), 1143. https://doi.org/10.1029/2002JA009489

Tetrick, S. S., Engebretson, M. J., Posch, J. L., Olson, C. N., Smith, C. W., Denton, R. E., et al. (2017). Location of intense electromagnetic ion cyclotron (EMIC) wave events relative to the plasmapause: Van Allen Probes observations. *Journal of Geophysical Research: Space Physics*, *122*(4), 4064–4088. https://doi.org/10.1002/2016JA023392

Thomsen, M. F. (2004). Why kp is such a good measure of magnetospheric convection. *Space Weather*, *2*(11), 2. https://doi.org/10.1029/2004SW000089

Thorne, R. M. (2010). Radiation belt dynamics: The importance of wave-particle interactions. *Geophysical Research Letters*, *37*(22), L22107. https://doi.org/10.1029/2010GL044990

Ukhorskiy, A. Y., Shprits, Y. Y., Anderson, B. J., Takahashi, K., & Thorne, R. M. (2010). Rapid scattering of radiation belt electrons by storm-time EMIC waves. *Geophysical Research Letters*, *37*(9), L09101. https://doi.org/10.1029/2010GL042906

Usanova, M. E., Mann, I. R., Bortnik, J., Shao, L., & Angelopoulos, V. (2012). THEMIS observations of electromagnetic ion cyclotron wave occurrence - dependence on AE, SYMH, and solar wind dynamic pressure. *Journal of Geophysical Research*, *117*(A10), A10218. https://doi.org/10.1029/2012JA018049

Usanova, M. E., Mann, I. R., Rae, I. J., Kale, Z. C., Angelopoulos, V., Bonnell, J. W., et al. (2008). Multipoint observations of magnetospheric compression-related emic Pc1 waves by Themis and Carisma. *Geophysical Research Letters*, *35*(L17S25), L17S25. https://doi.org/10.1029/2008GL034458

Wang, D., Yuan, Z., Yu, X., Deng, X., Zhou, M., Huang, S., et al. (2015). Statistical characteristics of emic waves: Van Allen probe observations. *Journal of Geophysical Research: Space Physics*, *120*(6), 4400–4408. https://doi.org/10.1002/2015JA021089

Wang, D., Yuan, Z., Yu, X., Huang, S., Deng, X., Zhou, M., & Li, H. (2016). Geomagnetic storms and EMIC waves: Van Allen probe observations. *Journal of Geophysical Research: Space Physics*, *121*(7), 6444–6457. https://doi.org/10.1002/2015JA022318

Wang, X. Y., Huang, S. Y., Allen, R. C., Fu, H. S., Deng, X. H., Zhou, M., et al. (2017). The occurrence and wave properties of emic waves observed by the magnetospheric multiscale (MMS) mission. *Journal of Geophysical Research: Space Physics*, *122*(8), 8228–8240. https://doi.org/10.1002/2017JA024237

Watari, S. (2017). Geomagnetic storms of cycle 24 and their solar sources. *Earth Planets and Space*, *69*(70), 70. https://doi.org/10.1186/s40623-017-0653-z

Wentworth, R. C. (1964). Enhancement of hydromagnetic emissions after geomagnetic storms. *Journal of Geophysical Research*, *69*(11), 2291–2298. https://doi.org/10.1029/JZ069i011p02291

Wygant, J., Bonnell, J. W., Goetz, K., Ergun, R. E., Mozer, F. S., Bale, S. D., et al. (2013). The electric field and waves instruments on the radiation belt storm probes mission. *Space Science Reviews*, *179*(1–4), 183–220. https://doi.org/10.1007/s11214-013-0013-7

Young, D. T., Perraut, S., Roux, A., de Villedary, C., Gendrin, R., Korth, A., et al. (1981). Wave-particle interactions near Ω_{He+} observed on GEOS 1 and 2: 1. Propagation of ion cyclotron waves inΩ_{He+}-rich plasma. *Journal of Geophysical Research*, *86*(A8), 6755–6772. https://doi.org/10.1029/JA086iA08p06755

Yu, X., Yuan, Z., Wang, D., Li, H., Huang, S., Wang, Z., et al. (2015). In situ observations of EMIC waves in O^+ band by the Van Allen Probe A. *Geophysical Research Letters*, *42*(5), 1312–1317. https://doi.org/10.1002/2015GL063250

Zhang, J., Halford, A. J., Saikin, A. A., Huang, C.-L., Spence, H. E., Larsen, B. A., et al. (2016). Emic waves and associated relativistic electron precipitation on 25–26 January 2013. *Journal of Geophysical Research: Space Physics*, *121*(11), 11086–11100. https://doi.org/10.1002/2016JA022918

Zhang, J.-C., Kistler, L. M., Mouikis, C. G., Dunlop, M. W., Klecker, B., & Sauvaud, J.-A. (2010). A case study of EMIC wave-associated He^+ energization in the outer magnetosphere: Cluster and Double Star 1 observations. *Journal of Geophysical Research*, *115*(A6), A06212. https://doi.org/10.1029/2009JA014784